The role of particle morphology on concrete fracture behaviour: A meso-scale modelling approach

Deheng Wei[a], Ryan C. Hurley[b], Leong Hien Poh[c], Daniel Dias-da-Costa[a], Yixiang Gan[a,*]

[a] *School of Civil Engineering, The University of Sydney, Sydney, Australia*
[b] *Department of Mechanical Engineering, Johns Hopkins University, Baltimore, USA*
[c] *Department of Civil and Environmental Engineering, National University of Singapore, Singapore*

ARTICLE INFO

ABSTRACT

Concrete is the most-used cementitious material and usually considered a three-phase composite with a mortar matrix, aggregates, and interfacial transition zones, all of which can fracture and even fragment. In this paper, the combined finite and discrete element method (FDEM) benchmarked with an in-situ X-ray micro-computed tomography and diffraction experiment is applied to bridge this gap in the meso-scale concrete fracture behaviour. To this end, algorithms are developed for realistic-shaped particle, packing, and high-quality FEM mesh-generation based on Voronoi tessellation and spherical harmonics. Using comprehensive simulations of virtually generated meso-scale concrete samples, it is found that rough particulates in concrete can increase its stress bearing capacity by enhancing intra-aggregate fracture paths. Results show that, the hierarchical aggregate morphology expressed by the fractal dimension more directly determines the compressive strength. Among the accessible conventional shape indices, convexity is the most effective parameter to correlate the global concrete fracture stress.

1. Introduction

In the context of particulate composites with second phase particles embedded in a host matrix material, the discrepancy of mechanical properties between the two phases can be used to produce superior overall material performance. For example, hard particulate inclusions can strengthen a non-composite matrix material, such as in metal matrices enhanced by ceramic particles [1,2]. In contrast, soft particulates can be distributed in a brittle matrix to enhance the universal fracture toughness [3]. Concrete is a typical example of a matrix-inclusion composite containing hard particulates. Its deformation, damage and failure can occur across the different length scales: macro, *meso*, micro and nano [4,5].

Macroscopically, there is no doubt that excellent progress has been achieved by representing concrete as a homogenous material. However, it is recognised to a certain extent that some mechanical properties, such as the inelastic deformation and brittle fracture behaviour, of heterogenous materials cannot be effectively captured by local continuum mechanics and linear elastic fracture models [6]. Despite the advancement and development of nonlocal continuum mechanics and nonlinear elastic fracture models [7–9], through which mean macro material responses can be described, the spatial variability of local

responses is difficult to capture [10]. The first level of concrete inhomogeneity can be found at the meso-scale, where the cementitious composite is a combination of coarse aggregates, interfacial transition zone (ITZ) and mortar paste for normal strength concrete. Fine aggregates and surrounding hardened cement paste hold the mortar paste. High strength concretes typically have low water to cement ratio (e.g. < 0.3 by mass) and may incorporate only mortar paste containing fine sands. Both of them, normal or high strength, are called concrete in some studies [73,96–98]. Up to now, most numerical studies meso-scale concrete using explicitly-generated particle shapes focus on normal strength concrete with coarse aggregates and mortar paste [24–29,42–44,53,65,66]. Due to the computational limitations, requiring similar mesh sizes for coarse and fine aggregates, the mortar paste must be treated as a homogeneous medium, which hinders investigation of fracture nucleation in finer-scale phases within the paste. In this study, we focus on the class of concretes without coarse aggregates, to reveal the interaction and competition of failure mechanisms between the cement paste matrix, fine aggregates and the ITZ, for compression induced fracture behaviour. The numerical framework can be extended for other classes of concretes with coarse aggregates, though at a significantly increased computational cost.

In the context of the prediction of mechanical properties for

---

* Corresponding author.
  E-mail address: yixiang.gan@sydney.edu.au (Y. Gan).

cementitious concrete, a major source of discrepancy with conventional composite theories [11], originates from the complexity of the interfacial transition zone (ITZ, e.g., [12,13]). For high strength concrete, the strengths of ITZ and mortar are widely assumed to be the same as aggregates [14], though actual measurement data remains scarce. Due to the experimental difficulties in controlling other factors of inclusions influencing the overall concrete strength (e.g. aggregate fabric, size, morphology and spatial distribution), the solid fraction of sand is widely adopted as the first primitive approximation for a net characterisation of these factors. Accordingly, contrasting findings appear in the literature. For example, when the aggregate volume fraction increased from 45% to 60%, Amparano et al. [15] indicate that the fracture energy and compressive strength would decrease, whereas Tasdemir and Karihaloo [16] conclude the opposite; Guinea et al. [17] found that rough aggregates can decrease the overall strength due to stress concentration at sharp corners, however in Wu et al.'s [14] experiments, 10–20% higher strength could be achieved using crushed quartzite instead of rounded marble aggregates. A plausible explanation for such an observation in Wu et al.'s experiments is that the stress concentration could induce cracks to propagate across harder aggregates when their morphology is rough, and hence more energy would be consumed when compared with fracturing along the relatively weaker ITZ and cement phase, therefore enhancing the overall compressive strength. In a short conclusion, experimental approaches at this scale are complex and difficult to control, particularly when attempting to isolate a single factor from the many other controllable and uncontrollable features.

A complementary tool to investigate the meso-scale fracture behaviour of concrete can be based on computational mechanics. In this scope, many works have explicitly depicted particle shapes using different approaches: molecular dynamics [18,19], DEM [20,21], FEM [22,23], FEM with various fracture models (e.g. cohesive element methods: [24,25]; phase field: [26,27]; and damage plasticity: [28,29]). Given its ability to describe discrete cracks, DEM is a promising approach for the purpose in this paper. Although the classical parallel bond DEM with rigid circular or spherical elements [30] may not be the most suitable for fracture simulation, due to its inherent limitations in describing elasticity and the fact that it requires the fitting of many local model parameters [31], many attempts have been made with DEM due to its novelty in dealing with the search and determination of contacts between fractured surfaces [32–34], considering that friction dissipates most input energy. To bypass the fractured surface contacting behaviour, most continuum-mechanics-based FEM simulations assume that tensile-induced behaviour and fractured surfaces after debonding would not contact intrinsically as encountered in DEM [35]. For meso-scale concrete simulations, where fracture can initiate and propagate in different phases, contact between fractured surfaces is an important feature of the underlying mechanisms.

Focusing on particles with regular or irregular morphology features, packing (for granular media) or parking (for cementitious materials) models for heterogenous composite materials can be classified into two main categories: real image-based and virtual computer-generated models. The former type of model takes real 2D pixels [27,36–37] or 3D voxels [38–40] as inputs and generates the corresponding computational model. This bottom-up method includes filtering for reducing noise of raw data, a threshold to separate different phases, and mesh generation for numerical methods (e.g. FEM and DEM). Each step of processing contains many parameters and nearly any of them can influence the final computational mechanics model to a certain degree. Further, besides the dependence on image resolution, the meshing of contacting aggregates is still a challenge. This is so because the approximation of the particle geometry would bring unavoidable intersections between contacting particles, which become unrealistic for meso-scale modelling. Some studies have directly implemented voxel data as the FEM mesh. However, after debonding, the contact between non-smooth voxelised surfaces becomes rather inaccurate. Even the

approximation for Herztian contact for contacting spheres may not be fully satisfactory [41].

In a top-down fashion, on the contrary, the computer-generated composite model firstly generates single aggregate shapes, and then park or pack them into a predefined domain. As early in 1980s, Zaitsev and Wittmann [42] pioneered the implementation of circular pores and circular or polygonal aggregates in 2D to simulate the fracture nucleation of meso-scale concrete, which attracted a number of subsequent studies [6,10,43,44]. Since then, more types of irregular particle shapes have been covered. Although many irregular shapes have been applied in recent computer-generated models, most are still far from being realistic and are completely convex for ease of contact detection. Considering the complexity of hierarchical particulate geometry, an effective shape parameter is required for describing its universal morphology features in addition to the conventional shape indices (e.g. aspect ratio, sphericity, convexity, roundness and roughness). The fractal dimension (D_f), a cross-scale descriptor that incorporates localised and overall particle morphological features, has the potential for serving as such a parameter [45,46].

Based on the above clarification, we are motivated to revisit the meso-scale concrete fracture behaviour with a specific focus on the role of particle morphology. The study is organised as follows. First in Section 2, a combined Spherical Harmonic (SH) analysis and Voronoi tessellation method is proposed to effectively produce realistic particle parking. Then, a combined finite and discrete element method (FDEM) approach is presented, where FEM with contact detection and interaction which is able to simulate not only the continuum behaviour within different phases, but also the initiation and development of internal cracks and the interactions between fractured parts, is adopted to simulate concrete fracture behaviour in Section 3. For the validation of the developed FDEM scheme, in-situ experimental XCT data of a meso-scale concrete sample is imported as a benchmark, including diffraction data for comparing aggregate stress tensors. For better clarity on the meaning and necessity of the simulations with virtual concrete specimen, additional inspirations from the in-situ experiment are also included. In Section 4, results of virtual meso-scale concrete simulations, focusing on various factors, such as aggregate volume fraction, particle morphology and particulate fabric, are discussed. Factors influencing concrete fracture behaviour are studied, highlighting the significant contributions from the particle morphology. Finally, discussions and conclusions are drawn in Section 5.

2. Generation of meso-scale concrete samples

In general, for non-overlapping particles via top-down fashion, there are 4 main methods for parking: i) the take-and-place method [24,47]; ii) size scaling method [48]; iii) Tetris method for minimum rectangle or cube particle boundary box [49]; and iv) Graph-based (e.g. Delaunay triangulation in 2D and Voronoi diagram in 3D) shrinking method [50,51]. By keeping the concept of DEM contact search [52] in mind, many dynamic packing methods, where particles are allowed to overlap slightly with one another, have been proposed [22,53]. When such methods are used, a further scaling of particles is needed after packing to eliminate overlapping from meshing. However, both existing parking and packing algorithms are mostly applicable for simplified particle shapes, and with the increase of particle vertices, they become significantly time-consuming [54–56]. On the other hand, due to the limited computational resources, meso-scale simulations must be performed on a representative volume element (RVE). Aggregates across RVE boundaries should be segmented, which is satisfied only by some research works containing simple-shaped inclusions [57,58]. When rough shapes comprising of many fine scale features are cut, a compromise must be made between merging short edges for computational efficiency and the retention of geometrical particle features.

Based on above discussions, this section presents the three-main parts of the procedure adopted for the generation of meso-scale

concrete samples. This procedure includes, along with the up-down algorithm, three main parts: Voronoi tessellation, Spherical Harmonic (SH) analysis and high-quality surficial mesh generation. First, the concrete domain is tessellated with a Voronoi tessellation, with the resulting cells becoming FEM elements. Compared with relevant research by Mollon and Zhao [55], the faces of the resulting FEM elements have a similar area, thereby avoiding distortions in SH expansion, and every Voronoi cell vertex is FEM node, well preserving cell geometry. For better reconstruction of cell surfaces, more vertices via sub-dividing FEM meshes are covered. Then, an SH analysis is conducted for every meshed cell, of which SH coefficients are subsequently altered to conform to the desired D_f and aspect ratio. The generated single particles are also scaled via their SH coefficients to be totally contained within the associated cell. At last, the SH coefficients are scaled by the given aggregate fraction. High-quality meshes are obtained by reconstructing particle geometry using spherical coordinates (θ, φ) from icosahedron-based geodesic sphere and unit octahedron-based geodesic sphere for complete and cut aggregates, of which the surface is composed of nearly uniform triangles.

2.1. Combined SH analysis and Voronoi tessellation

The distance $r_I (x_I(\theta, \varphi), y_I (\theta, \varphi), z_I (\theta, \varphi))$ between surface points on a star-shaped particle and the particle centroid in polar coordinate system, can be represented by the orthogonal Spherical Harmonic (SH) function:

$$r_I(\theta, \varphi) = \sum_{n=0}^{\infty} \sum_{m=-n}^{n} c_n^m Y_n^m(\theta, \varphi), \tag{1}$$

$$r_I(\theta, \varphi) = \sqrt{(x_I - x_0)^2 + (y_I - y_0)^2 + (z_I - z_0)^2}, \tag{2}$$

where I denoted the I-th selected node on the sub-divided cell mesh, (x_I, y_I, z_I) and (x_0, y_0, z_0) are the Cartesian coordinates of I-th node and the mass centre of the intact particle; $\theta \in [0, \pi]$ and $\varphi \in [0, 2\pi]$ are the latitudinal and longitudinal coordinates respectively, and c_n^m are the SH coefficients of degree n and order m. $Y_n^m(\theta, \varphi)$ ($n \in \mathbb{N}$, $-n \le m \le n$, $\mathbb{N}$ denotes natural number) is the so-called SH function defined on the surface of a sphere as:

$$Y_n^m(\theta, \varphi) = \sqrt{\frac{(2n+1)(n-|m|)!}{4\pi(n+|m|)!}} P_n^m(\cos\theta) e^{im\varphi}, \tag{3}$$

$$Y_n^{-m}(\theta, \varphi) = (-1)^m \left[\sqrt{\frac{(2n+1)(n-|m|)!}{4\pi(n+|m|)!}} P_n^m(\cos\theta) e^{im\varphi} \right]^*, \tag{4}$$

where $[.]^*$ denotes the complex conjugate and $P_n^m(x)$ are called associated Legendre functions, which can be expressed by Rodrigues' formula [59]:

$$P_n^m(x) = (1-x^2)^{\frac{|m|}{2}} \cdot \frac{d^{|m|}}{dx^{|m|}} \left[\frac{1}{2^n n!} \cdot \frac{d^n}{dx^n} (x^2-1)^n \right]. \tag{5}$$

The derivations and definitions of SH-based fractal dimension (D_f) are included in Appendix A. The relation between SH descriptors and degree n can be bridged by fractal dimension (D_f) as:

$$D_n = D_2 \cdot \left(\frac{n}{2} \right)^{2D_f - 6}, \tag{6}$$

where D_n is the SH descriptor defined by the normalized amplitude (L_n) of SH coefficient c_n by L_0 in Appendix A, where six kinds of commonly used concrete particulate materials demonstrate the novelty of SH D_f in denoting realistic aggregate morphology. The relative roughness (R_r) quantifying how globally different the irregular aggregate shape is from its c_0-determined sphere can be expressed as (see the derivation in Appendix A)

$$R_r = \sqrt{\sum_{n=2}^{n_{max}} \left(D_2 \cdot \left(\frac{n}{2} \right)^{2D_f - 6} \right)^2}, \tag{7}$$

from which it is clear that such aggregate roughness is dependent on both D_2 and D_f.

Given a domain $\Omega \in R^d$, d is the dimension, and it had N Voronoi cell points or generators, $\{p_i\}_{i=1}^N$, with its corresponding Voronoi tessellations or diagrams, $\{V_i\}_{i=1}^N$. The so-called Voronoi tessellation within specific domain can be generated [60]:

$$V_i = \{x \mid x \in \Omega \wedge \|x - p_i\| \le \|x - p_j\|, i \ne j, i, j \in [1, N] \wedge \mathbb{N}\}. \tag{8}$$

where i and j are i-th and j-th points of N; only if x belongs to the Voronoi cell boundary totally inside the domain boundary, $\|x - p_i\| = \|x - p_j\|$. Consequently, the whole domain is entirely discretised:

$$\begin{cases} \bigcup_{i=1}^{N} V_i = \Omega \\ V_i \cap V_j = \varnothing \end{cases}. \tag{9}$$

If the mass density of the domain or Voronoi tessellations is $\rho(x)$, the concurrent mass centre $\{m_i\}_{i=1}^N$ of single cell with its volume equal to v_i is

$$m_i = \frac{1}{v_i} \int_{v_i} x \cdot \rho(x) dx, i \in [1, N] \wedge \mathbb{N}. \tag{10}$$

To introduce the differences between cells of a domain, a geometry energy function is defined as:

$$\mathbb{E}(\{p_i\}_{i=1}^N, \{V_i\}_{i=1}^N) = \sum_{i=1}^{N} \int_{v_i} \|x - p_i\| \cdot \rho(x) dx. \tag{11}$$

Evidently, when $\{p_i\}_{i=1}^N$ coincides with $\{m_i\}_{i=1}^N$ the energy is the least and the cell geometry is the most stable. However, these two points are usually far from each other, and a perfect coincidence is rather difficult to be obtained. Iterations are applied to the easy case where $\{p_i\}_{i=1}^N$ is randomly distributed in the domain via moving generators of next loop to the mass centre of current cells:

$$\{\{p_i\}_{i=1}^N\}_{\mathbb{i}+1} = \{\{m_i\}_{i=1}^N\}_{\mathbb{i}}. \tag{12}$$

where $\mathbb{i}$ means $\mathbb{i}$-th loop or iterations. In this study, aggregate shapes are generated by the shrinking of Voronoi cells, via SH analysis, and are statistically similar, though not yet identical, to each other. With the given D_2 and D_f, the process to obtain temporary SH coefficients $\{c''_n\}_{i=1}^N$ of realistic aggregate shapes from those ($\{c'_{i,n}\}_{i=1}^N$) of Voronoi cells is given in Appendix B. To guarantee the aggregate to be completely contained in the cell, one can have:

$$\forall \{r_I(\theta, \varphi)\}_{i=1}^N \le \{d_I(\theta, \varphi)\}_{i=1}^N \tag{13}$$

where $d_I(\theta, \varphi)$ is the distance between cell surface vertices and its mass centre.

The scaling from mass centre for SH coefficients $\{c_{i,n}\}_{i=1}^N$ of final aggregate shapes must be done:

$$\{c_{i,n}\}_{i=1}^N \le \frac{\{c''_n\}_{i=1}^N}{\max\left(\left\{ \frac{r_I(\theta, \varphi)}{d_I(\theta, \varphi)} \right\}_{i=1}^N \right)}. \tag{14}$$

For further improving the efficiency of proposed framework in producing realistic particle shapes, five shape parameters are defined as:

$$\mathscr{F} = \frac{III}{II}; \tag{15}$$

$$\mathscr{E} = \frac{II}{I}; \tag{16}$$

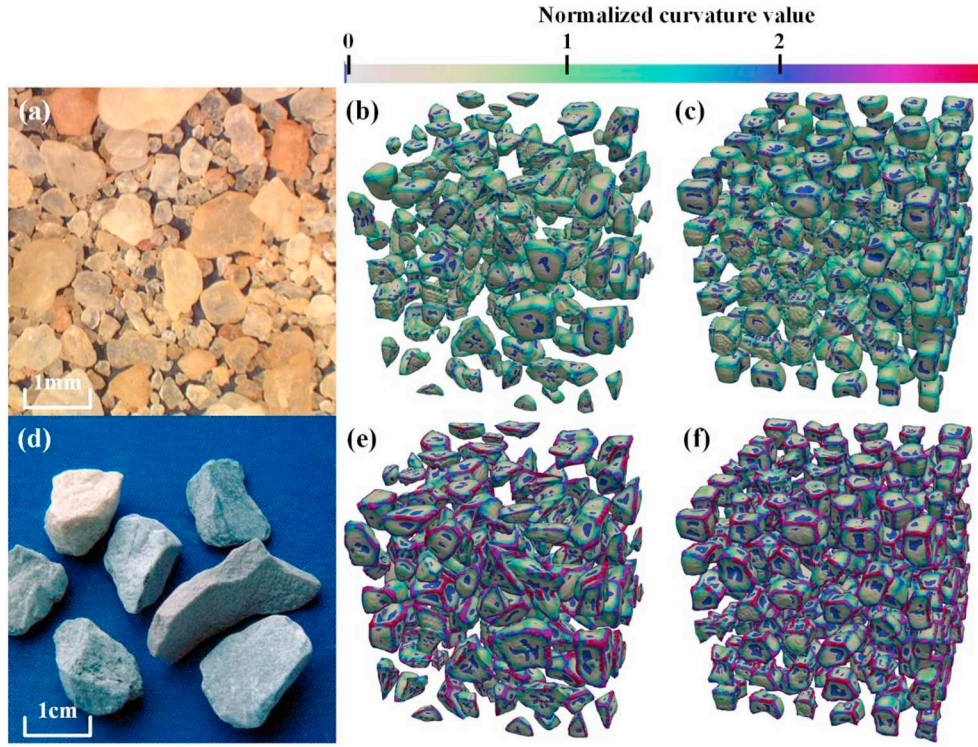$$\mathscr{S} = \frac{\sqrt[3]{36\pi \mathbb{V}_a^2}}{\mathbb{S}}; \tag{17}$$

Fig. 1. (a) and (d): Snapshots of real fine sand (MA-106A) and coarse sand (MA-1117) after [62], of which mean size is about 1 mm and 3 cm; (b) and (c): virtual fine sand packings from Voronoi cells after 0 and 100 iterations; (e) and (f): virtual coarse sand packings from Voronoi cells after 0 and 100 iterations. The colour bar denotes mean curvature value of vertices normalized by that of its correspondingly maximum sphere ($\frac{k_{M,l}}{k_{in}}$). (For interpretation of the references to colour in this figure legend, the reader is referred to the web version of this article.)

$$\mathscr{C} = \frac{\mathbb{V}_a}{\mathbb{V}_c}; \tag{18}$$

$$\mathscr{R} = \frac{\sum \left(\mathbb{S}_l \cdot \frac{k_{in}}{k_{M,l}} \right)}{\sum \mathbb{S}_l}, \ \forall \ k_{M,l} \le k_{in}, \tag{19}$$

where $\mathscr{F}$, $\mathscr{E}$, $\mathscr{S}$, $\mathscr{C}$ and $\mathscr{R}$ are shape indices of flatness, elongation, sphericity, convexity and roundness; I, II and III ($I > II > III$) denote the lengths of the longest, intermediate and shortest dimensions of the box exactly containing the aggregate using the Principal Component Analysis (PCA) in Matlab environment [94], respectively; $\mathbb{S}$ and $\mathbb{S}_l$ are the surface area of the aggregate and l-th triangular mesh to compose its surface; $\mathbb{V}_a$ and $\mathbb{V}_c$ are the volumes of the aggregate and its perfect convex hull; k_{in} is curvature value of the maximum inscribed sphere, while $k_{M,\,l}$ is the average of median curvature values of l-th triangle's three vertices [61].

A domain composed of 200 Voronoi cells is generated, of which the parental particles are two kinds of real sands, one coarse sand (MA-1117) and one fine sand (MA-106A) in Fig. A.1 of Appendix A. Fig. 1 illustrates the morphological features of the real and virtual particles, of which shape indices of virtual particulates are compared with their corresponding virtual samples in Fig. 2. The shape parameters of real aggregates in Fig. 2 are from an open-source software, Virtual Cement and Concrete Testing Library (VCCTL, Bullard, 2014). We use the Spherical Harmonic (SH) coefficients of various kinds of aggregates in VCCTL to conduct SH expansion in Eq. (1) and icosahedral geodesic structures with 1280 faces to reconstruct their shapes. Then, the parameters of the virtual aggregates are calculated according to Eqs. (15) to (19). D_f and D_2 conform to the fitted normal distributions of those from parental ones. Since the packing and generation of realistic-shaped aggregates are obtained from the shrinking process of Voronoi cells, the aggregate shapes are somewhat dependent on their corresponding cells, although irregular morphology features can be imposed via Spherical Harmonic (SH) analysis. According to properties of centroidal Voronoi tessellations [60], increasing iterations (moving generators of the next loop to the mass centre of current cells) makes the shapes and sizes of Voronoi cells more uniform. For example, if a large enough number of

iterations are made for a cubic domain containing L^3 generators, L^3 congruent cubic cells would be composing the whole region. Hence, the generated aggregates are more realistic than after 100 iterations in their spatial distributions, size distributions and shape parameters. One may expect the number of iterations for original Voronoi generators would much influence the shape parameters of the final particle shapes. However, from our quantitative results of shape indices of 200 particles in Fig. 2 and snapshots of virtual particle morphology in Fig. 1(b) to (c) and (e) to (f), such an influence is not too evident and a convergence tendency of particle shape indices appears with the increase of iterations of the initial Voronoi tessellations. Similar results, where Voronoi shapes have limited influence on shape parameters of their correspondingly realistic particles, have also been reported by [55], who first produce realistic-shaped particles and then put them into Voronoi cells. For coarse sands, clear angular faces can be seen from Fig. 1(d) while in Fig. 1(a) the fine sands have more curved surfaces. These key features also occurred in virtual samples from the high normalized curvature value ($\frac{k_{M,l}}{k_{in}}$) in Fig. 1(e) and (f). Notably, to facilitate the study on the effects of D_2 and D_f in concrete fracture behaviour, each aggregate had the same D_2 and D_f values in the following parts for the virtual concrete sample.

Voronoi tessellation has boundary effects since the cells connecting the domain boundary must have the boundary shapes of the domain [63]. To this end, as shown in Fig. 3(a), a larger periodic domain with size equal to $3\,L \times 3\,L \times 3\,L$ is defined for its uniformly distributed sub-boxes, each of size $L \times L \times L$. Ten iterations are first conducted in a sub-box having 64 random generators, which is more than the 24 aggregates for the RVE in composite theory [57]. The distributions of the Voronoi cell points are then copied into other 26 sub-domains. Finally, Voronoi cells are generated in the larger domain. Consequently, to avoid lengthy computation only cells including complete or cut aggregates are selected in Fig. 3(b), of which the entire concrete boundary is shown in Fig. 3(c).

2.2. Surface mesh generation

High-quality FEM mesh generation is still a big challenge to
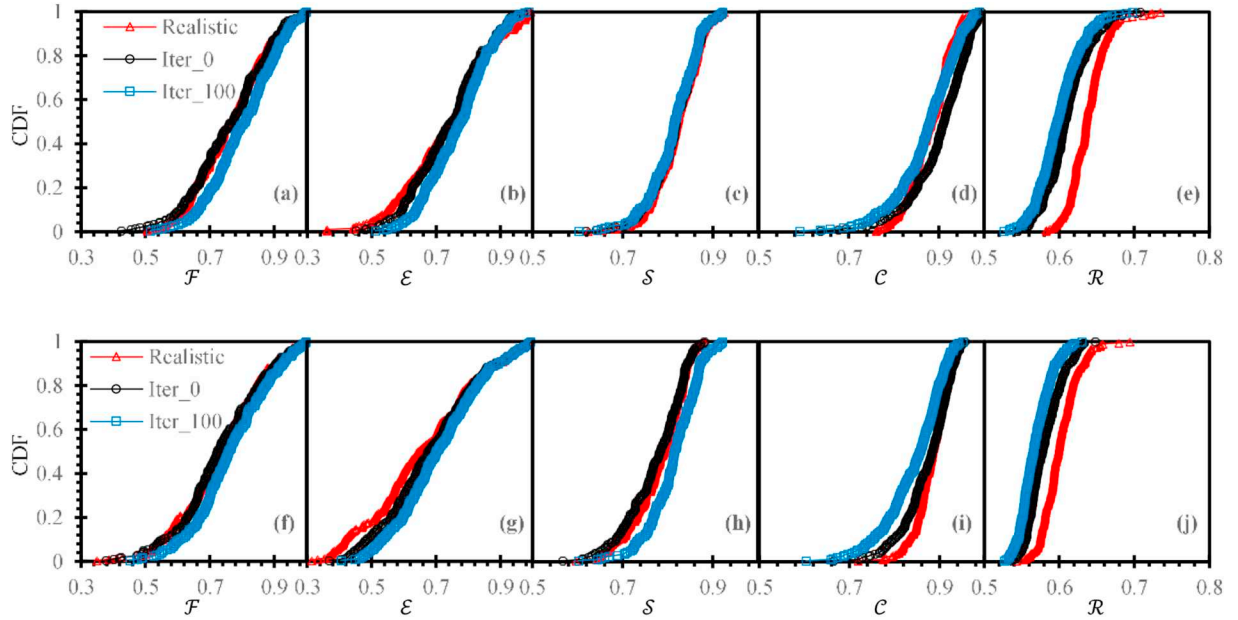
Fig. 2. Cumulative distribution functions (CDF) of various shape parameters for real and virtual fine ((a)–(e)) and coarse aggregates ((f)–(j)). $\mathscr{F}$, $\mathscr{E}$, $\mathscr{S}$, $\mathscr{C}$ and $\mathscr{R}$ denote flatness, elongation, sphericity, convexity and roundness.

successfully simulate meso-scale concrete fracture behaviour, especially for realistically shaped aggregates, for which four neighboured vertices do not fall on the same flat plane. This may be the reason why voxel data, after being re-scaled and resolution sacrificed, is implemented as a FEM cubic mesh for most XCT-based simulations [29,64,65]. Some researches [66,67] also generate a tetrahedral aggregate volume mesh via a mapping into an unstructured FEM mesh of the whole concrete. However, the resulting aggregate surface tomography is dependent on the pre-defined mesh of concrete, which is not sufficient for incorporating the influence of the aggregate morphology features. For example, even though diverse morphological details have been given to aggregates in terms of initial surficial meshes, the morphology would be transformed after mapping to that of pre-defined volume meshes. In this study, the generated aggregate mesh is first generated before the determination of cement paste matrix by cutting the aggregate mesh from the entire concrete domain.

One main advantage of SH-generated surfaces is the ability to reconstruct particle shapes based on the implicit form of aggregate boundary, as long as its SH coefficient is known in Eq. (1). On the other hand, to bypass the computational burden of FEM, an appropriate

number of high-quality surficial triangular meshes is needed. To mesh implicit boundary with SH function, many researches have implemented icosahedron-based geodesic spheres for this purpose [55,68], of which nodes are projected to those of implicit boundary with the same spherical angles. However, the gap between the number ($20 \times 4^{\aleph}$, $\aleph \in \mathbb{N}$) of meshes for this type of spherical angles is very long. Here, we approximate the arbitrary number of uniform triangular tessellating the unit sphere surface via searching for the minimum electrostatic energy [69]:

$$\mathbb{E} = \sum_{j=1}^{\aleph} \sum_{k=1}^{\aleph} \frac{q_j \cdot q_k}{\sqrt{d_{j,k}}}, j \neq k, \tag{20}$$

where $\aleph$ is the number of vertices on the sphere; q is the product of length and area distortion or the so-called particle charge; j and k denote j- and k-th vertex; d is the geodesic distance between two vertices. Appendixes C and D introduce surficial mesh generation of complete aggregates, as well as cut ones using octahedron-based geodesic structure. Fig. 4 shows the final surficial mesh of aggregates in the concrete sample. Clearly there are no short edges due to the cutting process, and
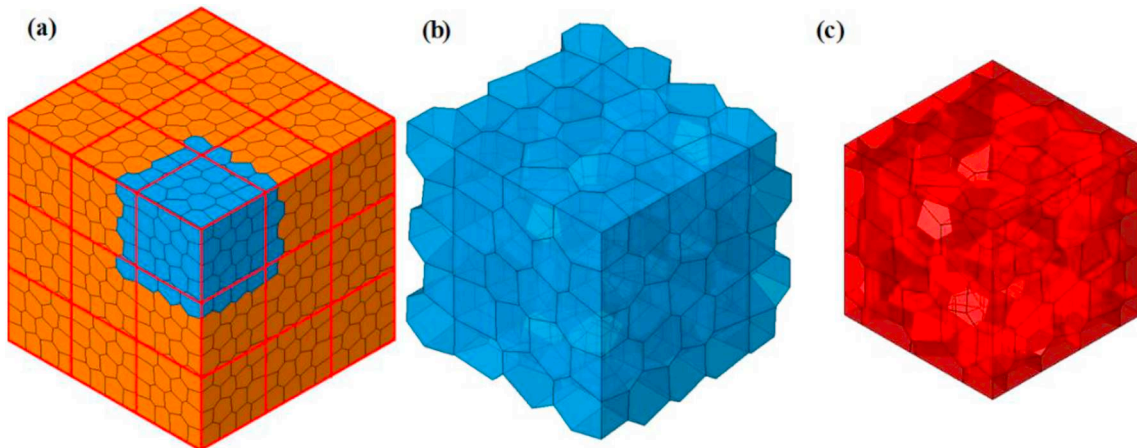
Fig. 3. Periodic Voronoi domain with 27 sub-domains (a), the enlargement of interest cells containing complete and cut aggregates (b) and cut Voronoi cells in the domain of concrete (c).
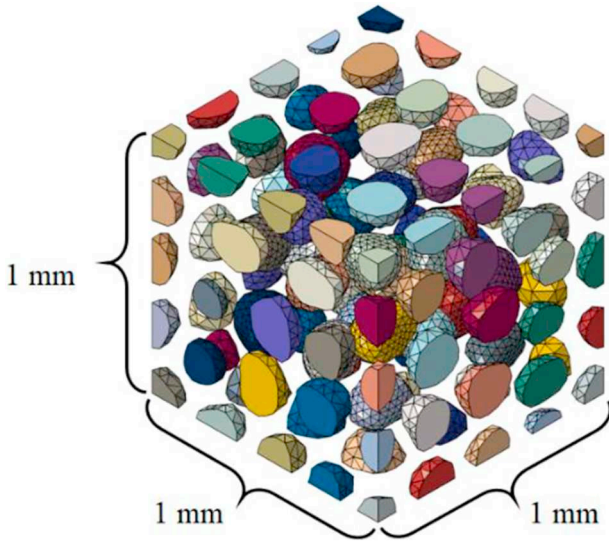
Fig. 4. Final surficial meshes of aggregates in concrete sample with size equal to 1 mm × 1 mm × 1 mm.

the mesh sizes of uncut aggregates are nearly identical to each other.

3. FDEM simulation and its validation

In this section the combined finite and discrete element method (FDEM) is briefly reviewed [70,71] and the key details are summarised. For more information please refer to a previous paper for single sand crushing behaviour [72]. The combined XCT and diffraction data from a uniaxial compression experiment on concrete [73] is also used as a benchmark for the simulations.

3.1. FDEM and its damage model

Within FDEM, solid parts are discretised using 4-noded tetrahedral FEM elements and the deformation and stress in them can be captured as in FEM, as shown in Fig. 5(a). Simultaneously, Fig. 5(b) shows the capability of DEM to deal with contact, thus FDEM can efficiently model the transition of continuum to discrete states, including the presence of fracture or even breakage of concrete. Although most aggregates undergo fracture, they can still bear a significant portion of the macro load due to their high strength, see Fig. 5(c). An explicit solver via central difference integration framework is adopted, due to its higher efficiency in dealing with a large number of contacts and deformation when compared with implicit solvers. A penalty function is implemented to calculate contact forces and prevent the overlapping of

contacting elements. Viscous damping, together with normal elastic response, is also introduced for numerical stability, while a Coulomb-type friction law is employed for friction forces. Fracture is simulated via the debonding of 6-node cohesive interfacial elements (CIEs) inserted between every two conjunct 4-node solid elements. In addition to solid aggregate elements used to simulate fracture of three-phase composed of concrete, another two kinds of CIEs and two types of solid elements are needed, see the experimental sample in Fig. 6 and corresponding solid aggregate elements in Fig. 7(d). After the deletion of the CIEs that have failed, completely fractured surfaces can still develop contact via the penalty function. The material failure process had two stages: fracture initiation and propagation. The maximum stress criterion, including tensile and shear strengths, is applied for crack initiation. Bilinear traction-separation damage laws are employed for the stiffness degradation during crack evolution. More details about the damage models are provided in Appendix E. For mixed damage-mode opening, the Benzeggagh-Kenane criterion [74] is employed:

$$
\begin{cases}
G_C = G_{n,C} + (G_{s,C} - G_{n,C})\left(\dfrac{G_{\text{shear}}}{G_T}\right)^{\eta}, \\
\quad G_{\text{shear}} = G_s + G_t \\
\quad G_T = G_n + G_s + G_t
\end{cases}
\tag{21}
$$

where $G_{n,C}$ and G_{shear} are the respective critical energies for pure mode I (tension) and combined modes II and III (shear), η is a material parameter, and G_T is the mixed fracture energy for the CIEs. For simplicity, we set $G_{s,\,C} = G_{n,\,C}$ and thus only $G_{n,\,C}$ influenced the energy-based crack evolution criterion.

Table 1 summarise the mechanical parameters adopted in this study. Note that the solid properties are taken from experimental researches by [75,76]; the stiffness values and mesh size are determined following [25,77]; other mechanical properties of CIEs are taken directly from relevant research by [77]; and the friction coefficient was 0.5.

Quasi-static loading conditions are approximated in the simulations by keeping kinetic energy below 10% of the associated internal energy. In this study, no loading platens are explicitly constructed, while the boundary conditions are set on the nodes at the top and bottom surfaces of the hexahedron concrete along loading direction, as in Fig. 5(a). The bottom surface is fixed in the loading direction, while the nodes at the top surface are applied a downward linearly ramp displacement velocity up to 0.04 m/s, which is then kept constant until an overall displacement of 0.1 mm was met. Nodes at both bottom and top surfaces are allowed to expand in other directions than loading direction.

3.2. In-situ experiment and its simulation

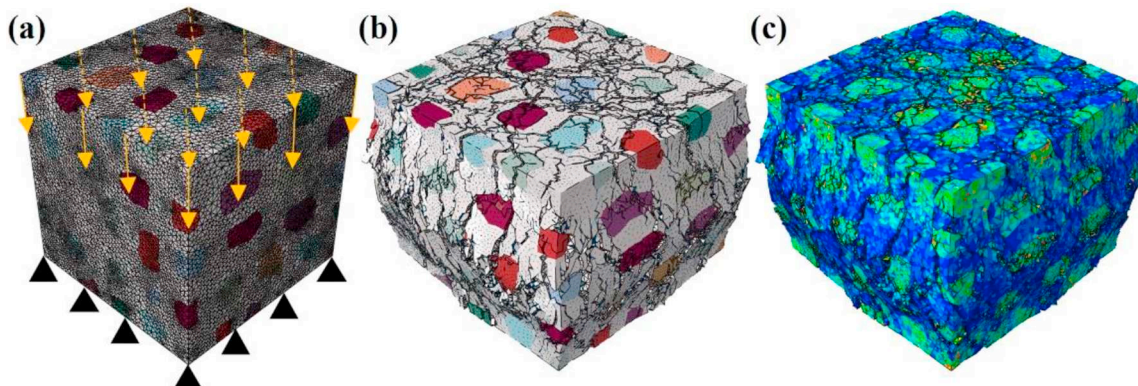The experimental uniaxial compressive test of a concrete sample

Fig. 5. (a) FEM meshes with displacement boundary conditions at top and bottom layer nodes, (b) fracture pattern and (c) stress contour of one typical virtual meso-scale concrete.
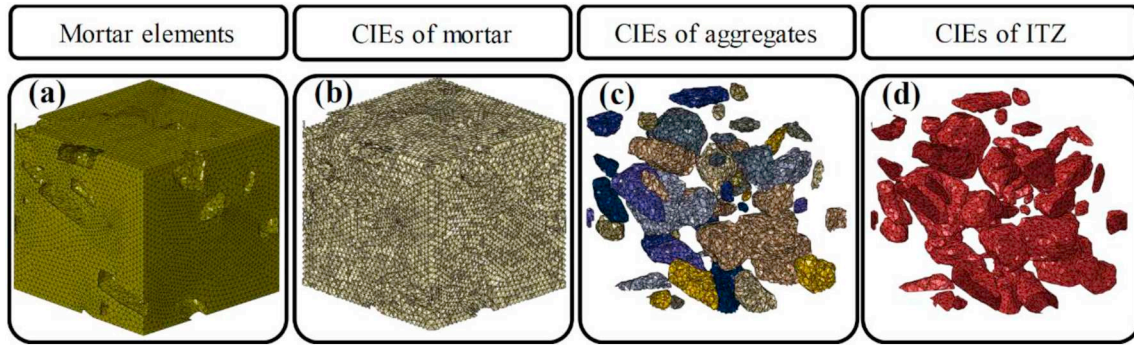
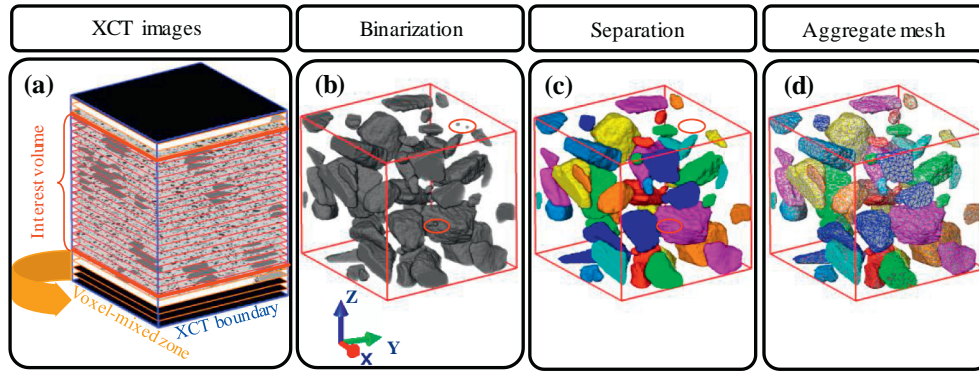Fig. 6. Different FDEM elements of the experimental sample of which aggregate elements are in Fig. 7(d).

Fig. 7. Image processing from XCT images to FEM mesh.

Table 1
FDEM material parameters of elements in concrete.

	Parameter	Value
Solid elements	Density, ρ (kg/m^3)	Agg: 2650
		CP: 2200
	Elastic modulus, E (GPa)	Agg: 96
		CP: 16
	Poisson's ratio, υ	Agg: 0.08
		CP: 0.23
Cohesive interface elements (CIEs)	Normal stiffness, k_n (N/m^3)	Agg: 9.6×10^{13}
		CP: 2.5×10^{13}
		ITZ: 1.36×10^{13}
	Shear stiffness, k_s (N/m^3)	Agg: 4.44×10^{13}
		CP: 1.04×10^{13}
		ITZ: 5.53×10^{13}
	Tensile strength, N_{max} (MPa)	Agg: 10
		CP: 4
		ITZ: 2.4
	Shear strengths, S_{max} and T_{max} (MPa)	Agg: 5
		CP: 2
		ITZ: 1.2
	Fracture energy, G_C (N/m)	Agg: 60
		CP: 50
		ITZ: 30
Contact law	Friction coefficient, μ	0.5

described in our recently published paper [73] is selected as the benchmark for the FDEM simulation. The size of the concrete sample was about 1 mm × 1 mm × 1 mm and it contains 52 small aggregates. For more information about the experimental procedures and sample preparation, please refer to [73]. At the experimental concrete boundary where the concrete sample contacted with the steel loading platens, a voxel-mixed zone with fuzzy 2D images occurred. Since the XCT images became unclear near the loading boundaries due to imaging artefacts, we heuristically cut out an interest volume that is about 85% of the full height of the sample, which is shown in Fig. 7(a). Given

that [73] used image processing to separate the different aggregate phases, in Fig. 7(b) the grey value intensities could be directly taken for binarization. However, there is still image noise that could be identified incorrectly as small 'aggregates', for example inclusions in the red ellipse of Fig. 7(b). These are removed after the labelling of various particulate phases in Fig. 7(c) by measuring and deleting all those small 'aggregates'. The volume ratio of the largest deleted small 'aggregate' to the smallest real aggregate was < 1%, which confirms that such deletions do not significantly alter the underlying composition. Finally, in Fig. 7(d) surficial meshes of different aggregates are generated with given numbers to retain a nearly linear relation between aggregate surface mesh number and surface area, using an open-source mesh tool, Iso2mesh [78]. Care is taken to avoid mesh intersection between touching aggregates, which are connected by ITZ CIEs, the same as the connection between aggregate and cement paste (CP) phases. The volume mesh of aggregates is produced using the open-source mesh tool Gmsh [79] with controlled mesh quality and number. Each simulation of the experiment and other virtual concrete samples involved about 350,000 solid and 700,000 cohesive elements. According to relevant studies of Wang et al. [24] having nearly identical number of aggregates to our model, 236,260 solid elements are found to be sufficient for the simulation of fracture behaviour of a meso-scale cubic concrete sample, from which the number of elements herein adopted are deemed adequate and no further mesh sensitivity studies are performed.

Notably, with the aid of XCT at a resolution of 1.48 μm, some initial voids were found in the experimental concrete sample, though at a low volume ratio of about 1%. Hence, voids are not considered in this study since the emphasis is on pure influences of particle morphology features. Fig. 8(a) illustrates the force-displacement curves of experiments and simulations. In experiments, the 1 mm^3 concrete sample, surrounded by aluminium cylinder to prevent fragments from being lost, was inserted into rotational and axial motion system (RAMS) loading grips at the Cornell High Energy Synchrotron Source (CHESS). The sample was compressed by lowering the stainless-steel platen in 2 μm

aggregates   **calcium silicates**   **cement paste**   **cracks or voids**
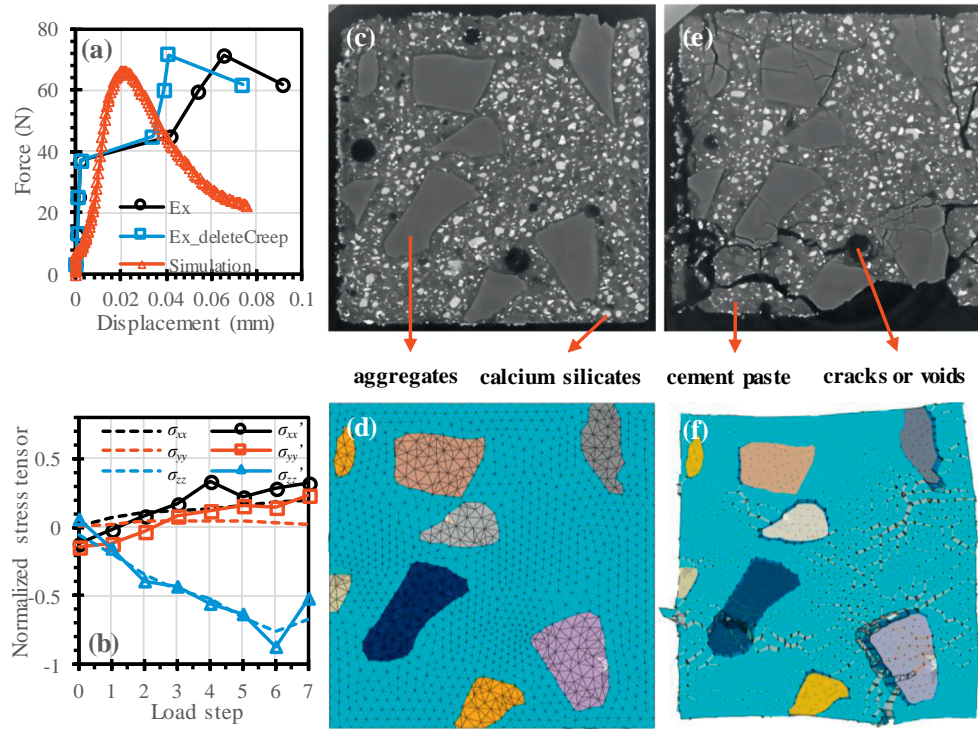
Fig. 8. Comparisons between simulations and experiments of the in-situ concrete fracture behaviour: (a) force-displacement curves; (b) evolutions of stress tensors with σ and σ' denoting aggregate stress tensors of simulations and experiments; (c) and (e) raw CT images without any image processing of the concrete before and after fracture and (d) and (f) associated FEM results before and after fracture with the same normalized forces by their maximum compression forces. The slice of XCT image in Fig. 8(c) is from the bottom of the cubic volume of interest and is highlighted by bold rectangular edges in Fig. 7(a).

increments until desired loads were reached. With the strain held constant, the concrete sample was rotated first 180° and then 360° for XCT and diffraction tests, respectively. The forces were obtained from the load cell; the sample stress was calculated by dividing the load cell reading during measurements by the initial sample area, 1mm².

For our FDEM numerical simulations of the experiments, the loading platens are not explicitly modelled and the boundary conditions are applied to bottom and up layers of nodes of the concrete sample, which are fixed only on loading directions. We are therefore confident that our calculated sample strain in all loading steps matched those in steps 4 to 7 in experiments.

It is plausible that relaxation occurs especially for the step with maximum displacement and the much longer scanning time due to the time required for experimental measurements, during which the upper loading platen is held in a fixed position to enable rotations of the sample aiming to conduct XCT and diffraction scan. The creep strains after this loading step are also calculated with the guidance of AS 3600:2018 [80] and then removed from Fig. 8(a). There are however still differences between the resulting curve and the numerical simulation. One reason for this phenomenon may be attributed to the roughness of sample surface planes in contact with the loading platens, on which newly observable fractures appear. From the raw XCT in Fig. 8(c) and (e) nearly every aggregate undergoes fracture and even breakage, indicating the necessity of their inclusion in the simulations of meso-scale concrete fracturing process. There are four different phases in them: voids or fractures, aggregates, cement paste and other high-density constituents. Black pixels with low greyscale values are deemed fractures or voids; white pixels with high greyscale values are for high-density constituents, such as calcium silicates; pixels with intermediate greyscale values denote cement paste or aggregates. Thresholds of grey values are carefully selected for segmenting phases, as described in [73]. A standard deviation filter is also used to threshold the aggregates from the cement paste, both of which have similar greyscale values (see [73] for details). Based on the fracture mechanics parameters for spherical aggregates in the meso-scale concrete simulation by [25], where no particle fracture is obtained, our simulations of in-situ experiments do exhibit aggregate fractures, as shown in Fig. 8(d)

and (f). Although there is no further calibration of parameters for the simulation of in-situ experiments, the fracture patterns between numerical and experimental results are comparable, as well as the force-displacement curves. It seems that the simulations underestimate intra-aggregate fracturing, when comparing Fig. 8(e) and (f). Two main reasons may explain it: First, as we have described in experimental procedures, during every load step of the experiment, the sample is kept at constant stress and strain during rotation for XCT and diffraction measurements. Considering that these operations take at least half an hour, additional fractures due to the time-dependent behaviour may occur. Meanwhile, in our computational simulations, no strain rate influence on fractures have been considered. Second, aggregates in our simulations are homogenous and defect free, while in experiments the aggregates are heterogenous and include natural flaws along which fractures can initiate and evolute. It is anticipated that fracture behaviour between simulations and experiments would be closer if these two problems are solved by using more advanced computational resources.

To compare stress of aggregates between simulations and experiments, volume-weighted stress tensors are defined as:

$$\sigma_{ij} = \frac{1}{\sum_{k=1}^{N_{agg}} V_{agg}^k} \cdot \sum_{k=1}^{N_{agg}} \sigma_{ij}^k V_{agg}^k, \tag{22}$$

where N_{agg} is the number of aggregates; k meant k-th aggregate; V and σ_{ij} are volume and stress tensors. Considering the differences between the numerical and experimental force-displacement curves, σ_{ij} is also normalized by F_{max}/A, where F_{max} was the peak force and A was the approximate horizontal cross-section area of the concrete (1 mm²). Load steps denoted by the same number in the simulation and the experiment are of the same normalized force with respect to their associated F_{max}. The main stress component σ_{zz}, towards the compression direction, nearly coincide with each other during loading process as shown in Fig. 8(b), which indicates the accuracy of the proposed FDEM schematic. The other two diagonal stress tensor components, σ_{xx} and σ_{yy}, have a similar evolution tendency in the numerical and experimental results.

4. The role of aggregate morphology

In this part, focus is given to the statistical analyses and discussions of the obtained results correlating particle morphology with concrete fracture behaviour. Three factors are discussed: D_f, aspect ratio in terms of D_2, and aggregate fraction. In real concrete, fine aggregate fraction in mortar is typically higher than in this study [95]. However, obtaining such high packing density of irregular-shaped particles is difficult. With the purpose of isolating the influence of the particle morphology on concrete fracture behaviour, we tried to eliminate other factors associated with particles, such as the particle size distribution, particle spatial position in the sample and its longest axis orientation. Generating densely-packed mono-sized aggregate fractions while ensuring that particle position and fabric (the longest axis orientation) remain unchanged in concrete containing different fine aggregate shapes is challenging. For this reason, and because the existing experimental data we used for validation is from a sample with an aggregate fraction of 20%, we keep the fine aggregate fraction of 20% for most simulations and focus on the relative contributions from the aggregate morphology on material behaviour.

The FEM meshes are generated via the combined Voronoi-SH framework presented in Section 2, and the FEM simulations are outlined in Section 3. To discuss the isolated influence of the features of the particle morphology or aggregate fraction (V_f), aggregates in all virtual concrete samples are produced from the same Voronoi cells to keep their mass centres, distributions, size and directions nearly identical. For different target V_f (e.g., 10%, 20% and 30%), every aggregate overlapping the cubic sample is scaled by the same factor ζ towards its mass centre, thus the final SH coefficient became

$$\{c_{i,n}\}_{i=1}^{N} = \{c_{i,n}\}_{i=1}^{N} \cdot \zeta, \tag{23}$$

$$\zeta = \sqrt[3]{\frac{V_{f,tar}}{V_{f,ini}}}, \tag{24}$$

where $\{c_{i,n}\}_{i=1}^{N}$ is the final SH coefficient for target V_f; $V_{f,\,tar}$ and $V_{f,\,ini}$ are the target and initial aggregate fraction. Then, $\{c_{i,\,n}\}_{i=1}^{N}$ is replaced by $\{c_{i,n}\}_{i=1}^{N}$ for the following steps in Section 2 for FEM mesh generation. In total, ten cases with different D_f, D_2 and aggregate fraction are depicted in Fig. 9. Fig. 10 illustrates stress-strain curves and the normalized crack areas of the three phases of the concrete.

According to [81], the energy release rate (G_c) in cohesive elements to simulate fracture propagation is mesh-size dependent to some extent; i.e. for increasing number of CIEs, the response may become more ductile, which is also observed by our previous research on single particle crushing simulations [72]. This study, however, is not aimed at solving this discrepancy but rather to identify and isolate the role of particle morphology on the concrete fracture behaviour. The aggregate

is kept with maximum surface area with exactly 400 surficial triangular meshes, which is also the number of ITZ CIEs. The relation between aggregate surficial mesh number and surface area is approximately linear, because the mesh number must be an integer. Completely cut aggregates at concrete boundary are of 128 surficial meshes without considering meshes of flat cut planes. It is to be noted that both numbers of aggregate surface meshes (triangles) and 4-node volume meshes (tetrahedrons) are in control. Overall, there are 350,000 solid and 700,000 cohesive elements of the whole domain via control global average solid element size.

When investigating the effect of D_f and D_2, the aggregate fraction is set to 20% which is nearly the same as the in-situ experiment, while D_f and D_2 are set to 2.1 and 0.3 for introducing the impact of aggregate fraction. Furthermore, a case with spherical aggregate fraction of 0.2 in Fig. 9(f) is also simulated for demonstration of stress concentrations induced by particle morphology. The size of the simulated concrete sample is kept the same as that of the experimental sample, and 64 complete or cut aggregates are contained in it.

4.1. Fractal dimension

Six cases are simulated for assessing the influence of D_f on the fracture behaviour of meso-scale concrete. One case considers spherical aggregates, whereas the other five are for $D_f = 2.1$ to 2.5, while all of them are of aggregate fraction equal to 0.2 and $D_2 = 0.3$. As depicted in Fig. 9(a)–(e), with the increase of D_f, the aggregate becomes rougher, which means more stress concentrations can occur at the boundaries of aggregates. In single point crushing tests, such stress concentration makes particles more prone to fracture [72]. As a result, rough aggregates increase the likelihood of aggregate fragmentation into finer fragments. Due to the higher strength and fracture energy of aggregates relative to those of cement paste and ITZ, a higher D_f therefore leads to more aggregate fracture during crack propagation. The overall concrete stress capacity, compressive strength, and toughness of concrete is therefore enhanced with higher D_f. Interestingly, the distribution of aggregates also influences the strength. For example, Kim and Al-Rub [82] simulate 4 cases with different random yet uniform distributions of identical spheres, and found around 5% variation of the peak stress. It is clear for the aggregates in Fig. 9 that the distribution and fabric or orientation of them is nearly identical, indicating the ease to distinguish the influence of aggregate morphology from its distribution on concrete fracture strength.

From the force-displacement curves in Fig. 10(a), the rough aggregate morphology does induce higher compressive strength. Kim and Al-Rub [82] apply in 2D circular, hexagonal, pentagonal, tetragonal and arbitrary polygonal shapes to discuss the influence of particle shapes. Therewith, the aggregate size distributions in various concrete
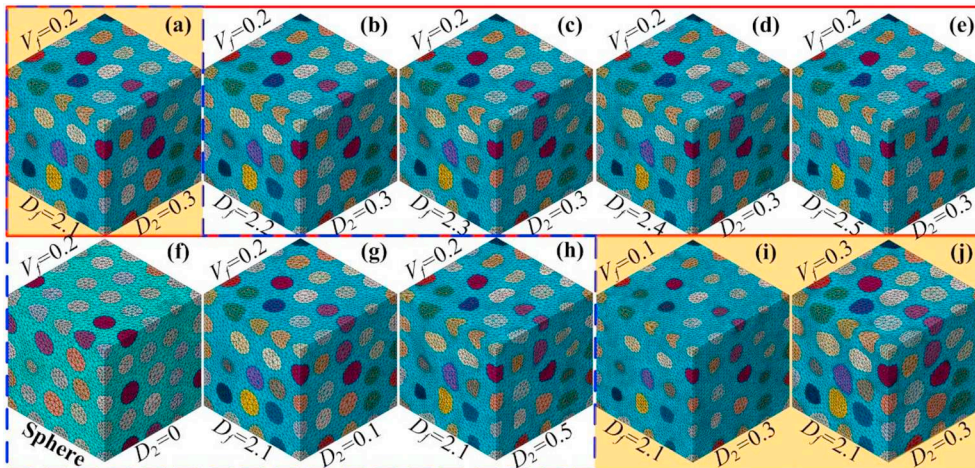

Fig. 9. Virtual meso-scale concrete samples with aggregates of different fractal dimension (D_f), aspect ratio determined by D_2 and aggregate fraction (V_f). Samples with red outlines, dashed blue outlines and yellow background are to investigate the isolated influence of D_f, D_2 and V_f, respectively. (For interpretation of the references to colour in this figure legend, the reader is referred to the web version of this article.)
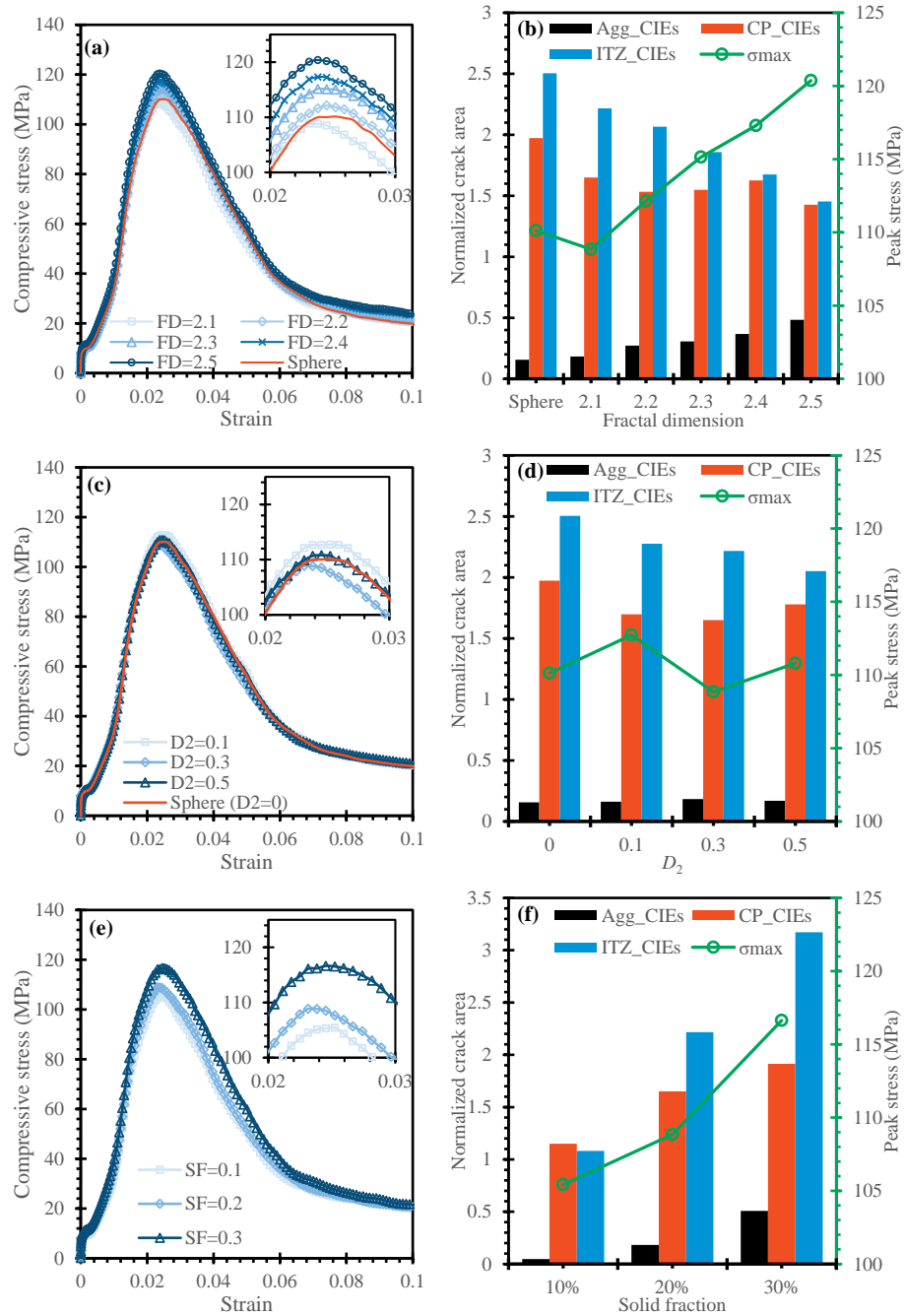
Fig. 10. Comparisons between the influence of different aggregate morphology focusing on various D_f (a–b), aspect ratio determined by D_2 (c–d) and aggregate fraction (e–f); (a), (c) and (e) are for stress-strain curves, while (b), (d) and (f) are for normalized crack area by concrete cross-section area (1mm^2) at corresponding peak stress.
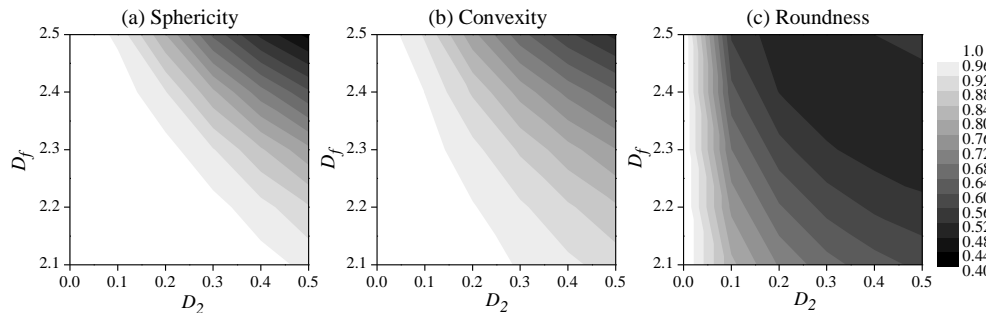
Fig. 11. Shape parameters evolution influenced by D_f and D_2: (a) sphericity, (b) convexity and (c) roundness.

samples are the same, while circular aggregates cause highest peak force. However, all the shapes in these cases are completely convex and have no roughness ($\mathscr{C} = 1$), and therefore have fewer stress concentrations than concave aggregates. Regarding morphology features in Fig. 9(a), aggregates with $D_f = 2.1$ are nearly completely convex with an average $\mathscr{C} = 0.9997$, while aggregates with $D_f = 2.5$ in Fig. 9(e) average $\mathscr{C} = 0.6306$. The relationships between $\mathscr{S}, \mathscr{C}$ and $\mathscr{R}$, and values of D_f and D_2 are shown in Fig. 11. This is the reason why the concrete of aggregates of $D_f = 2.1$ have lower strength than that of spherical aggregates in our simulations. On the contrary, in the recently published experimental work [83], the increase of roundness or sphericity (or decrease of fractal dimension) of four kinds of fine sands (Ottawa sand, Gabbro sand, MI sand and 2NS sand), which are all concave, would lower the overall concrete strength. This experimental finding enhances our simulations results, where aggregates in meso-scale concrete can improve the strength of it, even by about 10% when aggregate fractions are unchanged. In summary, both two seemingly contractive conclusions support our simulation findings.

To shed more light on meso-scale influences of aggregate morphology on concrete fracture behaviour, Fig. 10(b) represents the normalized crack area of three different completely fractured CIEs for the six cases. Interestingly, with increasing D_f of aggregates a competition mechanism exists between fractured ITZ and aggregates, which are the weakest and strongest phases in the concrete, while the medium-strength cement paste have less fluctuations. As the weakest phase in our sample, the ITZ is the most susceptible region to fracture. Naturally, fractures would propagate through the ITZ and along the boundary of rough aggregates. Rougher aggregates lead to a larger total area of ITZ but simultaneously generate more stress concentration on their surfaces. The latter provides more opportunities for cracks to begin propagating across aggregates. Consequently, with the increase of aggregate roughness, in terms of D_f, the area of fractured ITZ decreases, while the area of fractured aggregate increases. This finding microscopically explained the reason why macro strength of concrete with rough aggregates is enhanced.

4.2. Aspect ratio determined by D_2

In the perspective of SH-generated aggregates and to the extent of global particle morphology, D_2 mainly introduces aggregate aspect ratios, reflected in Fig. 9(f), (g), (a) and (h) for $D_2 = 0$, 0.1, 0.3 and 0.5, respectively. Four simulated cases are of the same aggregate fraction and D_f (0.2 and 2.1). Compared with D_f-induced variations of peak stress in Fig. 10(a), D_2 affects peak forces much less, as shown in Fig. 10(c). Simultaneously, in Fig. 10(d) the competition mechanism between fractures in aggregates and ITZ almost vanish, while a low variation of cement paste crack area is observed as before. Considering the shape anisotropy of aggregates, contrasting conclusions could be found in previous relevant researches. For example, Wang et al. [24] report that with an increased irregularity of aggregate shapes (e.g. spherical, ellipsoidal and polyhedral shapes), the strength of concretes with identical aggregate fraction decrease. In contrast, Xu and Chen [84] find an opposite trend on the influence of aggregate shape. In their case, the aggregates are packed via a random taking and placing algorithm; therefore, except for grading aggregate spatial distribution, aggregate fabric and orientation are not controlled. Hence, the impact of particle shape cannot be isolated from other key factors governing meso-scale concrete facture behaviour.

Meanwhile, there is no apparent relation between compressive strength and aggregates' D_2 values from our simulations. For the cases studied, the most irregular aggregates generated via $D_2 = 0.5$ have a mean value of $\mathscr{C} = 0.9494$. Therefore, an increase in D_2 for the cases considered does not significantly increase the underlying stress concentration effect, which explains the negligible variation in macro strengths although the fractured ITZ decreases slightly.
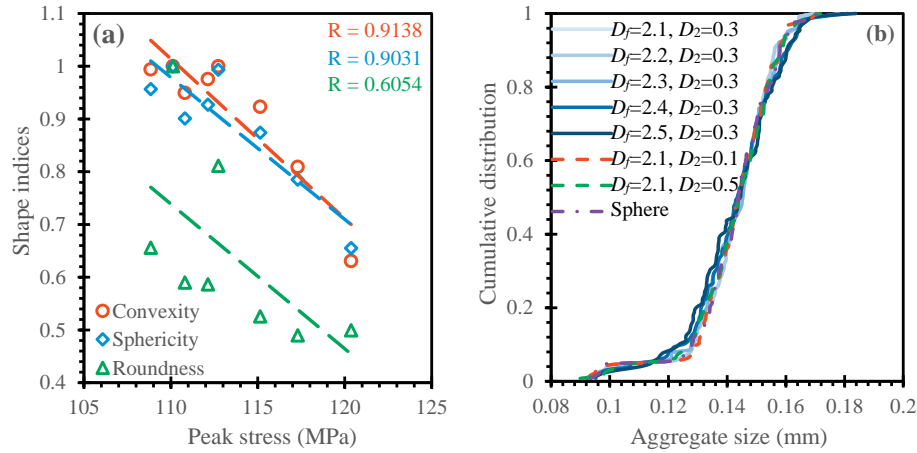
4.3. Aggregate fraction

Due to the difficulty in controlling particle morphology features and particle distributions, and the reality where there are no two particles with completely identical morphology, the influence of the aggregate fraction has been investigated by many numerical and experimental studies mostly with randomly distributed aggregates. In this section, 3 cases, in Fig. 9(i), (a) and (j), of aggregate volume fraction (V_f) equal to 10%, 20% and 30%, with $D_f = 2.1$ and $D_2 = 0.3$, are simulated. The non-overlapping aggregates with $D_f = 2.1$ and $D_2 = 0.3$, generated via combined Voronoi cell and SH analysis method in Section 2, have the initial V_f equal to 41.9%. The target V_f is generated by scaling the initial $\{c_{i,\ n}\}_{i=1}^N$ value according to Eqs. (23) and (24). Xu et al. [37] investigate the influence of solid fraction of realistically shaped aggregates on 2D meso-scale concrete strength and conclude that a larger aggregate fraction could enhance concrete strength. In contrast, Wang et al. [24] demonstrate with 3D simulations that increasing spherical, ellipsoidal or polyhedral aggregate volume fractions would lower the concrete strength. Interestingly, Kim and Al-Rub [82] report that for concretes with circular aggregates, the relations between strength and aggregate fraction is roughly bilinear, and a minimum global strength is achieved when the aggregate fraction is about 0.4. It is to be noted that the aggregate distributions and orientations in their simulations are random and aggregate fracture is not taken into consideration, although they have also acknowledged that the two factors can impact concrete strength [82].

To consider the severely localised damage due to aggregate fraction rather than morphology, Fig. 10(e) represents that with the increase of solid fraction from 0.1 to 0.3 via scaling aggregate sizes, concrete strength does grow about 10%. Aggregates in these samples have variations in their aggregate size, while maintaining the same morphological features. Wu et al. [14] point out that concrete strength would be improved with crushed limestone rather than natural round sand of the same material. According to the explanation in Section 4.1, this improvement is due to higher angularity or convexity of crushed limestone, compared to intact limestone. Microscopically, due to the increase of surface area rather than aggregate roughness, fracture areas of the three phases increase, while cracks in aggregates increase most significantly. However, some construction aggregate materials, especially for those without long-time natural abrasion to generate rounded global shape (e.g. recycled concrete aggregate), would not have much increase in universal convexity after the re-crushing process. Hence, it is practical to assume that the concrete strength made from this kind of crushed materials would not be significantly reduced. Although recycled concrete aggregates with fractured mortar on it have weaker strength than rounded natural sands, their size and morphology are larger and rougher. Silva et al. [85] experimentally clarify that the recycled aggregate concrete tends to exhibit a comparable strength with that of the corresponding natural aggregate concrete. In contrast, because of the higher convexity of crushed natural aggregates, we conclude that concretes made from crushed natural aggregate would have higher strength than those made from recycled fragmented aggregate, since the bulk properties of the ITZ in the two types of concrete are similar [86].

4.4. Discussions about aggregate selection in concrete

From the studies presented in this paper, it is clear that particle shape deserves more attention in concrete design. Unfortunately, it is not yet feasible to scan the large amounts of sand in concrete in 3D mainly due to its cost and operational constraints. Recently, Su and Yan [87] have pointed out that for a typical sand, among other parameters, convexity has the best linear correlation between its 2D and 3D values. With the increasingly easy access to digital cameras and development of 2D shape quantification algorithms [88], referring to 2D shape parameters to provide a quick guidance about choosing specific aggregates

Fig. 12. (a) Relations between peak forces and shape parameters; and (b) aggregate size distributions for aggregate fraction equal to 0.2. Aggregate size is approximated by diameter of its volume-equivalent sphere.

becomes possible. Fig. 12(a) illustrates the relations between peak forces and mean shape measurements for cases with particulate fraction equal to 0.2, and the corresponding aggregate size distributions are represented in Fig. 12(b). The good match between lines show that the grading dependence [89] in concrete fracture mechanics has been eliminated. Such a tendency in our simulations is not only consistent with the experiments of [83], but also covers more kinds of sand particle shapes via combined Voronoi tessellation and SH analysis.

5. Conclusions

A combined FDEM approach is used to simulate concrete fracture focusing on the particle shape effects. A combined XCT and diffraction experiment of uniaxial concrete under compression is used as benchmark and validation, and an advanced realistic-shaped aggregate packing algorithm is proposed. Although compromises are made between both aggregate fraction and controllable particle size, and spatial position and fabric, and the findings may be quantitatively different for higher aggregate fraction, the 30% maximum aggregate fraction in our simulations, lower than real concrete, is comparable with those of similar studies of parking of poorly graded simple ellipsoidal and polyhedron particles. By adding overlapping detection algorithms, it is possible that high solid fraction (e.g. > 0.5) could be efficiently obtained by scaling the particle size. Since the adjacent Voronoi cells share one face, overlapping detection is necessary for vertices only, which have the same initial Voronoi cell FEM surficial vertex coordinates, of neighbour particles. The results and findings presented in this study provide valuable insight on the fracture mechanisms of concrete at the meso-scale. Following this study, the following main conclusions are highlighted:

- The simulations using the aggregate packing algorithm provide advantages for probing the meso-scale concrete fracture behaviour with controllable factors (e.g. fractal dimension, distributions and fabric) of realistic particle shapes to highlight the importance of aggregate morphology, which would be inaccessible in experiments.
- At the meso-scale level and for the same aggregate fraction, the fracture stress of concrete could be directly enhanced by about 10% by adopting rough aggregates with lower convexity, whereas

changing their aspect ratio may not influence concrete strength as much.
- There is a competition mechanism between the fracture of the ITZ and aggregates. With increasing aggregate roughness, fracture may propagate across aggregates instead of along ITZ due to stress concentration, whereas the fracture of cement paste seemed to be less affected.
- For concrete made of recycled construction materials, of which aggregate roughness would not remarkably increase after crushing, high aggregate fraction may enhance its global strength, if ITZ strengths for high and low aggregate fractions were identical.

CRediT authorship contribution statement

Deheng Wei: Conceptualization, Methodology, Formal analysis, Visualization, Investigation, Writing - original draft.**Ryan C. Hurley:**Formal analysis, Resources, Validation, Investigation, Writing - review & editing.**Leong Hien Poh:**Investigation, Writing - review & editing.**Daniel Dias-da-Costa:**Formal analysis, Investigation, Writing - review & editing.**Yixiang Gan:**Supervision, Conceptualization, Methodology, Investigation, Writing - review & editing.

Declaration of competing interest

The authors declare that they have no known competing financial interests or personal relationships that could have appeared to influence the work reported in this paper.

Acknowledgements

Appendix A. Derivations of SH-based fractal dimension

This part is mainly about SH-based fractal dimension (D_f) to characterise particle morphology. For the single degree n, there are $2n + 1$ complex numbers of SH coefficients to be determined according to Eq. (1), hence when the user-defined maximum degree is n_{max}, the whole set of SH coefficients c_n^m include $(n_{max} + 1)^2$ complex numbers. Due to the orthonormal properties of the SH function, the more general calculation of c_n^m to reconstruct or smooth target particle shapes follows the integral

$$c_n^m = \int_0^{2\pi} \int_0^{\pi} sin\,\theta \cdot r(\theta, \varphi) \cdot [Y_n^m(\theta, \varphi)]^* d\theta d\varphi. \tag{A.1}$$

Two following important properties of SH coefficients can be deduced from Eqs. (3) and (4):

$$c_n^m = (-1)^m \cdot (c_n^m)^*, \tag{A.2}$$

$$c_n^0 \in R, \tag{A.3}$$

where R denotes real number. Generally, the higher the $n_{\max}$ is, the finer object scales would be represented.

The amplitude at each SH frequency can be measured by

$$L_n = \sqrt{\sum_{m=-n}^{n} \|c_n^m\|^2}, \ (n = 0 \cdots 15), \tag{A.4}$$

where $\|.\|$ is the L_2 norm and L_n values are also normalized by L_0 to eliminate the influence of particle volume. Moreover, because L_1 does not influence much the SH-reconstructed particle morphology as that in 2D Fourier transformation [55], L_1 is set to 0. At last, the so-called SH descriptors are defined as:

$$\begin{cases} D_0 = 1 \\ D_n = L_n/L_0, \ (n = 2, 3, 4, 5...) \end{cases}. \tag{A.5}$$

As in Fig. A.1, the exponential relations between D_n and n of wide ranges of real particulates have been found that:

$$D_n \propto n^\beta, \tag{A.6}$$

where $\beta = -2H$ is the slope of the regression plot of log (D_n) versus log (n) and H was the Hurst coefficient that is related to the Fractal Dimension (D_f) of Fourier transformation by the following expression [90]:

$$D_f = 3 - H = (6 + \beta)/2. \tag{A.7}$$

By substituting Eq. (A.6) into Eq. (A.7), the remaining SH descriptors can be quantified by:

$$D_n = D_2 \cdot \left(\frac{n}{2}\right)^{2D_f - 6}. \tag{A.8}$$

Roughness of one specific particle surface is also defined. Starting with Parseval's formula and orthogonality of SH function, mean square distance (MSD) can be defined as [68]

$$MSD = \frac{1}{4\pi} \sum_{n=0}^{\infty} \sum_{m=-n}^{n} \|c_n^m\|^2. \tag{A.9}$$

Roughness existing on a surface is not meaningless, when it is compared with a specific surface. If the SH coefficients of two compared surfaces are $c_{1,n}$ and $c_{2,n}$, the global differences between them can be defined as root mean square distance (RMSD),

$$RMSD = \sqrt{\frac{1}{4\pi} \sum_{n=0}^{\infty} \sum_{m=-n}^{n} \|c_{1,n}^m - c_{2,n}^m\|^2}. \tag{A.10}$$

Due to the periodicity of spherical angles, $\int_0^{2\pi} \int_0^{\pi} r(\theta, \varphi) d\theta d\varphi$ is rotational invariant. *RMSE* is also rotational invariant. If the roughness is defined as how different it is from it c_0-determined sphere, we obtain:

$$c_{2,n} = c_{1,n}^0. \tag{A.11}$$

It is also necessary to normalize the roughness by the c_0-determined sphere:

$$R_r = \frac{\sqrt{\frac{1}{4\pi} \sum_{n=1}^{n_{max}} \sum_{m=-n}^{n} \|c_n^m\|^2}}{c_0^0 \cdot Y_0^0(\theta, \varphi)}. \tag{A.12}$$

where R_r is the defined relative roughness. Then Eqs. (A.4)–(A.5) and (A.8) in Appendix A are imported into Eq. (4), the relations between R_r and D_2 and D_f are:

$$R_r = \frac{\sqrt{\frac{1}{4\pi}\left(L_1^2 + \sum_{n=2}^{n_{max}} \left(c_0^0 \cdot D_2 \cdot \left(\frac{n}{2}\right)^{2D_f - 6}\right)^2\right)}}{c_0^0 \cdot Y_0^0(\theta, \varphi)}. \tag{A.13}$$

Since L_1 is set to zero and $Y_0^0(\theta, \varphi) = \frac{1}{2\sqrt{\pi}}$, R_r reads

$$R_r = \sqrt{\sum_{n=2}^{n_{max}} \left(D_2 \cdot \left(\frac{n}{2}\right)^{2D_f - 6}\right)^2}. \tag{A.14}$$

Considering $n_{max} = 15$ in this study, it is clear that if two of R_r, D_2 and D_f are known, the third is determined automatically. In other words, global particle roughness is dependent on both D_2 and D_f.

As a result, the multi-scale aggregate morphology features are compressed into two parameters, namely D_2 and D_f. Although in the previous study [46], the linear relation between SH descriptor and degree n in log-log scales has been illustrated, only two kinds of sand particles are contained, and they are of the similar size (e.g. the equivalent-volume-sphere is from 0.5 mm to 2 mm). For further improving, six kinds of particles, as shown in Fig. A.1, in concrete and with size laying in larger scopes (e.g. from fine sands to coarse aggregate) from Virtual Cement and Concrete Testing Laboratory (VCCTL, [62]) are covered. Again, it is proven that the SH-based D_f enabled the description of hierarchical particle morphological features.
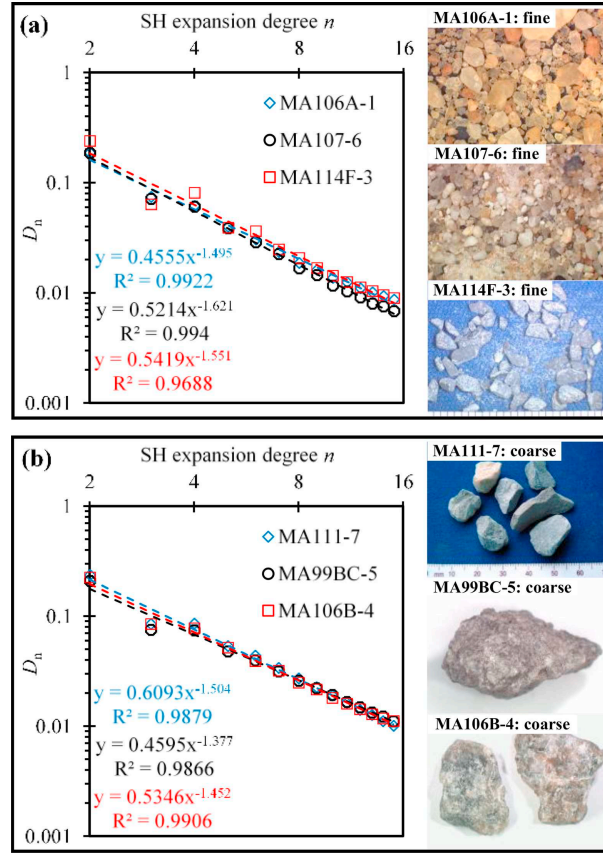
Fig. A.1. The relations between SH descriptor D_n and SH expansion degree for six kinds of granular materials used in concrete (adopted from [62]): (a): fine sands; (b): coarse aggregates.

Appendix B. From SH-reconstructed Voronoi cells to realistic aggregate shapes

As aforementioned, after meshing Voronoi cells and reconstructing them, the SH coefficients $\{c'_{i,n}\}_{i=1}^N$ of each Voronoi cells can be obtained:

$$
\{c'_n\}_{i=1}^N =
\begin{pmatrix}
\{c'_{i,0}\}_{i=1}^N \\
\{c'_{i,1}\}_{i=1}^N \\
\vdots \\
\{c'_{i,n-1}\}_{i=1}^N \\
\{c'_{i,n}\}_{i=1}^N \\
\{c'_{i,n+1}\}_{i=1}^N \\
\vdots \\
\{c'_{i,25}\}_{i=1}^N
\end{pmatrix}^T
$$

$$
=
\begin{pmatrix}
\{c'_{i,0}\}_{i=1}^N \\
(\{c'^{-1}_{i,1}\}_{i=1}^N \quad \{c'^{0}_{i,1}\}_{i=1}^N \quad \{c'^{1}_{i,1}\}_{i=1}^N)^T \\
\vdots \\
(\{c'^{-(n-1)}_{i,n-1}\}_{i=1}^N \quad \cdots \quad \underbrace{\{c'^{0}_{i,n-1}\}_{i=1}^N}_{2\times(n-1)+1} \quad \cdots \quad \{c'^{n-1}_{i,n-1}\}_{i=1}^N)^T \\
(\{c'^{-n}_{i,n}\}_{i=1}^N \quad \cdots \quad \underbrace{\{c'^{0}_{i,n}\}_{i=1}^N}_{2\times n+1} \quad \cdots \quad \{c'^{n}_{i,n}\}_{i=1}^N)^T \\
(\{c'^{-(n+1)}_{i,n+1}\}_{i=1}^N \quad \cdots \quad \underbrace{\{c'^{0}_{i,n+1}\}_{i=1}^N}_{2\times(n+1)+1} \quad \cdots \quad \{c'^{n+1}_{i,n+1}\}_{i=1}^N)^T \\
\vdots \\
(\{c'^{-25}_{i,25}\}_{i=1}^N \quad \cdots \quad \underbrace{\{c'^{0}_{i,25}\}_{i=1}^N}_{2\times 25+1} \quad \cdots \quad \{c'^{25}_{i,25}\}_{i=1}^N)^T
\end{pmatrix}^T .
$$

(B.1)

Then for a given D_2 and D_f, via scaling $\{c'_{i,n}\}_{i=1}^N$ using real numbers, the SH coefficients $\{c''_{i,n}\}_{i=1}^N$ of temporary aggregate shapes can be obtained from:

$$\{c''_n\}_{i=1}^N = \begin{pmatrix} \dfrac{\{D''_{i,0}\}_{i=1}^N}{\{D'_{i,0}\}_{i=1}^N}\cdot\{c'_{i,0}\}_{i=1}^N \\[2mm] (0\quad 0\quad 0)^T \\ \vdots \\ \dfrac{\{D''_{i,n-1}\}_{i=1}^N}{\{D'_{i,n-1}\}_{i=1}^N}\cdot\underbrace{\left(\{c'^{-(n-1)}_{i,n-1}\}_{i=1}^N \quad \cdots \quad \{c'^{0}_{i,n-1}\}_{i=1}^N \quad \cdots \quad \{c'^{n-1}_{i,n-1}\}_{i=1}^N\right)^T}_{2\times(n-1)+1} \\ \dfrac{\{D''_{i,n}\}_{i=1}^N}{\{D'_{i,n}\}_{i=1}^N}\cdot\underbrace{\left(\{c'^{-n}_{i,n}\}_{i=1}^N \quad \cdots \quad \{c'^{0}_{i,n}\}_{i=1}^N \quad \cdots \quad \{c'^{n}_{i,n}\}_{i=1}^N\right)^T}_{2\times n+1} \\ \dfrac{\{D''_{i,n+1}\}_{i=1}^N}{\{D'_{i,n+1}\}_{i=1}^N}\cdot\underbrace{\left(\{c'^{-(n+1)}_{i,n+1}\}_{i=1}^N \quad \cdots \quad \{c'^{0}_{i,n+1}\}_{i=1}^N \quad \cdots \quad \{c'^{n+1}_{i,n+1}\}_{i=1}^N\right)^T}_{2\times(n+1)+1} \\ \vdots \\ \dfrac{\{D''_{i,25}\}_{i=1}^N}{\{D'_{i,25}\}_{i=1}^N}\cdot\underbrace{\left(\{c'^{-25}_{i,25}\}_{i=1}^N \quad \cdots \quad \{c'^{0}_{i,25}\}_{i=1}^N \quad \cdots \quad \{c'^{25}_{i,25}\}_{i=1}^N\right)^T}_{2\times 25+1} \end{pmatrix}^T .$$

(B.2)

where $\{D''_n\}_{i=1}^N$ and $\{D'_n\}_{i=1}^N$ can be calculated using Eq. (14).

Appendix C. Details of surficial mesh generation

According to Euler's formula in topology,

$$\aleph + \mathfrak{f} - \mathfrak{e} = 2,$$ (C.1)

where $\aleph$, $\mathfrak{f}$ and $\mathfrak{e}$ read the number of vertices, faces and edges of the approximated sphere. Since one edge is shared by two triangles, $\aleph$ can be written as:

$$\aleph = \frac{\mathfrak{f}}{2} + 2.$$ (C.2)

Firstly, $\aleph$ vertices are randomly distributed on the surface of the sphere. Then iterations are conducted by moving the position of each vertex, in descending orders of their contribution in Eq. (20), along the negative gradient and then onto unit sphere surface:

$$\{\{\boldsymbol{x}_j\}_{j=1}^\aleph\}_{i+0.5} = \{\{\boldsymbol{x}_j\}_{j=1}^\aleph\}_{i} - \alpha\left[\frac{\partial \mathfrak{C}}{\partial\{\{\boldsymbol{x}_j\}_{j=1}^\aleph\}_i} - \left(\{\{\boldsymbol{x}_j\}_{j=1}^\aleph\}_i\cdot\frac{\partial \mathfrak{C}}{\partial\{\{\boldsymbol{x}_j\}_{j=1}^\aleph\}_i}\right)\{\{\boldsymbol{x}_j\}_{j=1}^\aleph\}_i\right],$$ (C.3)

$$\{\{\boldsymbol{x}_j\}_{j=1}^\aleph\}_{i+1} = \frac{\{\{\boldsymbol{x}_j\}_{j=1}^\aleph\}_i + 0.5}{\|\{\{\boldsymbol{x}_j\}_{j=1}^\aleph\}_i + 0.5\|},$$ (C.4)

where $\mathfrak{i}$ meant the $\mathfrak{i}$-th iteration; $\boldsymbol{x}_j = (x_{j,1}\quad x_{j,2}\quad x_{j,3})^T$ is the position vector of j-th vertex on the unit sphere surface; α is the step size and defined as 10^{-3}, here. Every triangle-approximated sphere is obtained after 1000 iterations. Notably, the closed-form of Eq. (C.3) is hard to obtain, of which approximation of $\frac{\partial \mathfrak{C}}{\partial\{\{x_j\}_{j=1}^\aleph\}_i}$ is written in Appendix D. Fig. C.1 shows spheres with 36, 396 and 3996 nearly uniform distributed triangular meshes, respectively.
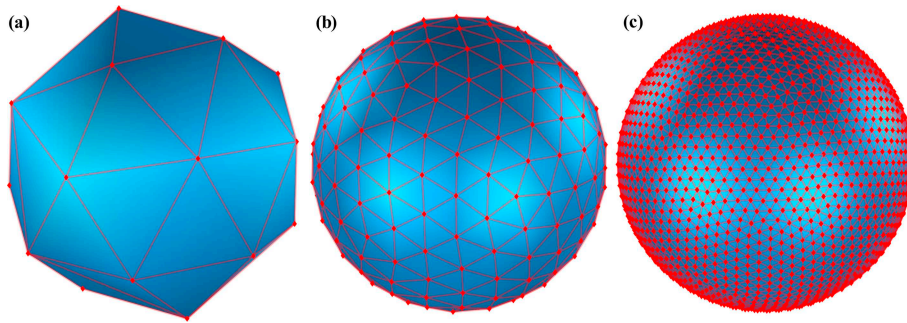

Fig. C.1. Snapshots of spheres with nearly uniform triangular meshes with different number of vertices: (a) 20; (b) 200; and (c) 2000.

Due to the setting up of RVE structures, some aggregates crossed by the concrete boundary are cut. Some short edges are unavoidable and made computation costs higher. Although such short edges can be merged via altering the flat surface induced by cut planes, stress concentrations in the alternations can hinder the usage of the RVE. For these aggregates, an octahedron-based geodesic structure is applied to reconstruct their surficial meshes, as in Fig. C.2(a). Submitting Eq. (1) into transformation matrix from spherical to Cartesian coordinates:

$$\begin{cases} x_I(\theta,\varphi) = \sin\theta\cdot\cos\varphi\sum_{n=0}^\infty\sum_{m=-n}^n c_n^m Y_n^m(\theta,\varphi) \\ y_I(\theta,\varphi) = \sin\theta\cdot\sin\varphi\sum_{n=0}^\infty\sum_{m=-n}^n c_n^m Y_n^m(\theta,\varphi), \\ z_I(\theta,\varphi) = \cos\theta\sum_{n=0}^\infty\sum_{m=-n}^n c_n^m Y_n^m(\theta,\varphi) \end{cases}$$ (C.5)

it is evident that when $\varphi = 0, \frac{\pi}{2}, \pi$ and $\frac{3\pi}{2}$ and $\theta = 0$ and π, three orthogonal planes could be achieved, and the three planes crossed each other at the original coordinate which is also set as the 'centre' of aggregate on the corner of the concrete. The 'centre' of other cut aggregate is selected on the cut plane. As in Fig. C.2(b) and (c), changing reconstruction centre of this type of realistic star-like aggregates would little alter its morphology, while short cut edges are avoided.
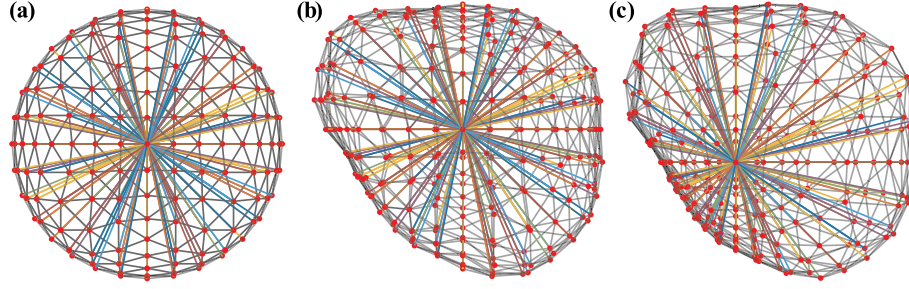
Fig. C.2. (a): octahedron-based geodesic mesh; (b): particle surface mesh produced by triangular topology relations from (a); and (c): particle surface mesh reconstructed from shifted 'centre'.

Appendix D. Approximation of $\frac{\partial \mathsf{C}}{\partial \{\{x_j\}_{j=1}^{\aleph}\}_i}$

Vertex charge is a function of its position and can be described by linear interpolation,

$$q_j = q(\{x_j\}_{j=1}^{\aleph}) = uq_{j,1} + vq_{j,2} + wq_{j,1}. \tag{D.1}$$

where u, v and w are the spherical barycentric coordinates of x_j, hence with $\{A_j\}_{j=1}^{\aleph} = [\{x_{j,1}\}_{j=1}^{\aleph} \ \{x_{j,2}\}_{j=1}^{\aleph} \ \{x_{j,3}\}_{j=1}^{\aleph}]$,

$$\{A_j\}_{j=1}^{\aleph} \cdot [u \ \ v \ \ w]^T = \{x_j\}_{j=1}^{\aleph}, \ u, v, w \geq 0, u + v + w \geq 1. \tag{D.2}$$

Via the triangle intersection meshing algorithm in [69], an approximation of C is obtained:

$$\frac{\partial \mathsf{C}}{\partial \{\{x_j\}_{j=1}^{\aleph}\}_i} \approx 2 \sum_{j \neq k}^{\mathfrak{A}_j} \frac{q_j}{d_{j,k}} \left[\begin{array}{c} \dfrac{adj(\{A_j\}_{j=1}^{\aleph})}{det(\{A_j\}_{j=1}^{\aleph})} \cdot [q_{j,1} \ \ q_{j,2} \ \ q_{j,3}] \\[1.5em] + \dfrac{q_j \{x_j\}_{j=1}^{\aleph} \{x_k\}_{k=1}^{\aleph}}{d_{j,k} [1 - (\{x_j\}_{j=1}^{\aleph} \cdot \{x_k\}_{k=1}^{\aleph})^2]^2} \{x_k\}_{k=1}^{\aleph} \end{array} \right]. \tag{D.3}$$

where adj (.) and det (.) denote the adjoint and determinant matrices; $\mathfrak{A}_j = \{k \mid \{x_j\}_{j=1}^{\aleph} \cdot \{x_k\}_{k=1}^{\aleph} \geq \cos\gamma\}$, and $\gamma = \frac{\pi}{4}$ is the threshold value of angle separation in this study.

Appendix E. Damage models of CIEs
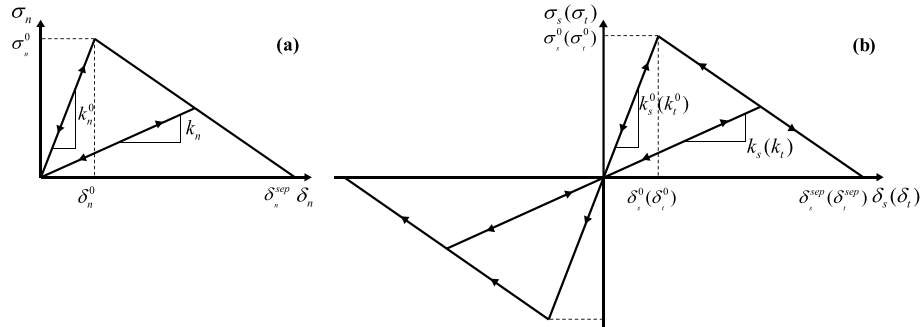
Fig. E.1. Bilinear constitutive relations of CIEs: (a) Normal component; (b) Shear components.

Traction-separation damage laws [91,92] are implemented to simulate the fracture of CIEs. Bilinear functions are defined for the relation between cohesive zone displacement and traction force, as in Fig. E.1:

$$\sigma = \begin{pmatrix} \sigma_n \\ \sigma_s \\ \sigma_t \end{pmatrix} = \mathbf{K}\boldsymbol{\delta} = \begin{pmatrix} k_{nn} & k_{ns} & k_{nt} \\ k_{sn} & k_{ss} & k_{st} \\ k_{tn} & k_{ts} & k_{tt} \end{pmatrix} \begin{pmatrix} \delta_n \\ \delta_s \\ \delta_t \end{pmatrix}, \tag{E.1}$$

where $\boldsymbol{\sigma}$ is the traction stress vector, $\mathbf{K}$ is the elasticity matrix, $\boldsymbol{\delta}$ is the relative displacement matrix, and n, s and t denote the normal and two shear directions. Off-diagonal components of the elastic matrix $\mathbf{K}$ are set to zero. The relative displacements are defined as:

$$\delta_{n,s,t} = \varepsilon_{n,s,t} T, \tag{E.2}$$

where ε is the strain along the three directions for the CIEs and T is the fictitious thickness herein set as 1 for the equality of nominal strain to its corresponding displacement.

The constitutive response of the CIEs covers two main stages, i.e., before and after breakage initiation. The maximum nominal stress criterion is

applied to identify the breakage initiation in three phases of concrete as suggested in [93]:

$$\max\left\{\frac{<\sigma_n>}{N_{\max}}, \frac{\sigma_s}{S_{\max}}, \frac{\sigma_t}{T_{\max}}\right\}, \tag{E.3}$$

where $N_{\max}$, $S_{\max}$ and $T_{\max}$ are the failure stress of CIEs, and $<\cdot>$ is the Macaulay bracket, by which compressive stress is set to 0 and not considered as a source of breakage at micro-scale.

After crack initiation, contact stiffness reduces according to partial interface damage, and the stress-displacement relationship is updated by Fig. E.1:

$$\sigma_n = \begin{cases} k_n\delta_n, \ \delta_n \geq 0 \\ k_n^0\delta_n, \ \delta_n < 0 \end{cases}, \tag{E.4}$$

$$\sigma_s = k_s\delta_s, \tag{E.5}$$

$$\sigma_t = k_t\delta_t, \tag{E.6}$$

where $k_{n,\,s,\,t} = (1 - D)k_{n,\,s,\,t}^0$. D is the damage variable for linear damage evolution defined as:

$$D = \frac{\delta_m^{\mathrm{sep}}(\delta_m^{\max} - \delta_m^0)}{\delta_m^{\max}(\delta_m^{\mathrm{sep}} - \delta_m^0)}, \tag{E.7}$$

$$\delta_m^{\mathrm{sep}} = \frac{2G_C}{\sigma_{\mathrm{eff}}^0}, \tag{E.8}$$

$$\sigma_{\mathrm{eff}}^0 = \sqrt{<\sigma_n>^2 + \sigma_s^2 + \sigma_t^2}, \tag{E.9}$$

where δ_m^{sep} and δ_m^0 are the corresponding displacements for complete failure and crack initiation, $\delta_m^{\max}$ is the maximum displacement registered during the loading history, σ_{eff}^0 is the relatively effective traction stress at crack initiation, and G_C is the Griffith fracture energy for crack evolution.

References

[1] J. Li, B.Y. Zong, Y.M. Wang, W.B. Zhuang, Experiment and modeling of mechanical properties on iron matrix composites reinforced by different types of ceramic particles, Mater. Sci. Eng. A 527 (29–30) (2010) 7545–7551.

[2] T. Christman, A. Needleman, S. Suresh, An experimental and numerical study of deformation in metal-ceramic composites, Acta Metall. 37 (11) (1989) 3029–3050.

[3] L.S. Sigl, P.A. Mataga, B.J. Dalgleish, R.M. McMeeking, A.G. Evans, On the toughness of brittle materials reinforced with a ductile phase, Acta Metall. 36 (4) (1988) 945–953.

[4] M. Vandamme, F.J. Ulm, Nanogranular origin of concrete creep, Proc. Natl. Acad. Sci. 106 (26) (2009) 10552–10557.

[5] F.J. Ulm, M. Vandamme, H.M. Jennings, J. Vanzo, M. Bentivegna, K.J. Krakowiak, K.J. Van Vliet, Does microstructure matter for statistical nanoindentation techniques? Cem. Concr. Compos. 32 (1) (2010) 92–99.

[6] Z.P. Bažant, M.R. Tabbara, M.T. Kazemi, G. Pijaudier-Cabot, Random particle model for fracture of aggregate or fiber composites, J. Eng. Mech. 116 (8) (1990) 1686–1705.

[7] G. Sun, L.H. Poh, Homogenization of intergranular fracture towards a transient gradient damage model, Journal of the Mechanics and Physics of Solids 95 (2016) 374–392.

[8] J.Y. Wu, A unified phase-field theory for the mechanics of damage and quasi-brittle failure, Journal of the Mechanics and Physics of Solids 103 (2017) 72–99.

[9] L.A. Le, G.D. Nguyen, H.H. Bui, A.H. Sheikh, A. Kotousov, Incorporation of micro-cracking and fibre bridging mechanisms in constitutive modelling of fibre reinforced concrete, Journal of the Mechanics and Physics of Solids 133 (2019) 103732.

[10] A. Zubelewicz, Z.P. Bažant, Interface element modeling of fracture in aggregate composites, J. Eng. Mech. 113 (11) (1987) 1619–1630.

[11] R.M. Christensen, Mechanics of Composite Materials, Wiley, New York, 1979.

[12] E.J. Garboczi, Permeability, diffusivity, and microstructural parameters: a critical review, Cem. Concr. Res. 20 (4) (1990) 591–601.

[13] H. Zhang, B. Šavija, S.C. Figueiredo, E. Schlangen, Experimentally validated multi-scale modelling scheme of deformation and fracture of cement paste, Cem. Concr. Res. 102 (2017) 175–186.

[14] K.R. Wu, B. Chen, W. Yao, D. Zhang, Effect of coarse aggregate type on mechanical properties of high-performance concrete, Cem. Concr. Res. 31 (10) (2001) 1421–1425.

[15] F.E. Amparano, Y. Xi, Y.S. Roh, Experimental study on the effect of aggregate content on fracture behavior of concrete, Eng. Fract. Mech. 67 (1) (2000) 65–84.

[16] M.A. Tasdemir, B.L. Karihaloo, Effect of aggregate volume fraction on the fracture parameters of concrete: a meso-mechanical approach, Mag. Concr. Res. 53 (6) (2001) 405–415.

[17] G.V. Guinea, K. El-Sayed, C.G. Rocco, M. Elices, J. Planas, The effect of the bond between the matrix and the aggregates on the cracking mechanism and fracture parameters of concrete, Cem. Concr. Res. 32 (12) (2002) 1961–1970.

[18] F. Sanchez, K. Sobolev, Nanotechnology in concrete–a review, Constr. Build. Mater. 24 (11) (2010) 2060–2071.

[19] G. Xu, H. Wang, Study of cohesion and adhesion properties of asphalt concrete with

[20] M. Nitka, J. Tejchman, A three-dimensional meso-scale approach to concrete fracture based on combined DEM with X-ray μCT images, Cem. Concr. Res. 107 (2018) 11–29.

[21] N.H. Nguyen, H.H. Bui, S. Arooran, G.D. Nguyen, J. Kodikara, Discrete element method investigation of particle size distribution effects on the flexural properties of cement-treated base, Comput. Geotech. 113 (2019) 103096.

[22] P. Sheng, J. Zhang, Z. Ji, An advanced 3D modeling method for concrete-like particle-reinforced composites with high volume fraction of randomly distributed particles, Compos. Sci. Technol. 134 (2016) 26–35.

[23] X. Zhu, Y. Gao, Z. Dai, D.J. Corr, S.P. Shah, Effect of interfacial transition zone on the Young's modulus of carbon nanofiber reinforced cement concrete, Cem. Concr. Res. 107 (2018) 49–63.

[24] X. Wang, M. Zhang, A.P. Jivkov, Computational technology for analysis of 3D meso-structure effects on damage and failure of concrete, Int. J. Solids Struct. 80 (2016) 310–333.

[25] O. Yılmaz, J.F. Molinari, A mesoscale fracture model for concrete, Cem. Concr. Res. 97 (2017) 84–94.

[26] T.T. Nguyen, J. Yvonnet, M. Bornert, C. Chateau, Initiation and propagation of complex 3D networks of cracks in heterogeneous quasi-brittle materials: direct comparison between in situ testing-microCT experiments and phase field simulations, Journal of the Mechanics and Physics of Solids 95 (2016) 320–350.

[27] Z.J. Yang, B.B. Li, J.Y. Wu, X-ray computed tomography images based phase-field modeling of mesoscopic failure in concrete, Eng. Fract. Mech. 208 (2019) 151–170.

[28] P. Grassl, H.S. Wong, N.R. Buenfeld, Influence of aggregate size and volume fraction on shrinkage induced micro-cracking of concrete and mortar, Cem. Concr. Res. 40 (1) (2010) 85–93.

[29] Y. Huang, Z. Yang, W. Ren, G. Liu, C. Zhang, 3D meso-scale fracture modelling and validation of concrete based on in-situ X-ray computed tomography images using damage plasticity model, Int. J. Solids Struct. 67 (2015) 340–352.

[30] D.O. Potyondy, P.A. Cundall, A bonded-particle model for rock, Int. J. Rock Mech. Min. Sci. 41 (8) (2004) 1329–1364.

[31] D. André, J. Girardot, C. Hubert, A novel DEM approach for modeling brittle elastic media based on distinct lattice spring model, Comput. Methods Appl. Mech. Eng. 350 (2019) 100–122.

[32] N.H. Nguyen, H.H. Bui, G.D. Nguyen, J. Kodikara, S. Arooran, P. Jitsangiam, A thermodynamics-based cohesive model for discrete element modelling of fracture in cemented materials, Int. J. Solids Struct. 117 (2017) 159–176.

[33] N.H. Nguyen, H.H. Bui, G.D. Nguyen, J. Kodikara, A cohesive damage-plasticity model for DEM and its application for numerical investigation of soft rock fracture properties, Int. J. Plast. 98 (2017) 175–196.

[34] N.H. Nguyen, H.H. Bui, J. Kodikara, S. Arooran, F. Darve, A discrete element modelling approach for fatigue damage growth in cemented materials, Int. J. Plast. 112 (2018) 68–88.

[35] F. Fan, J. Choo, A phase-field method for modeling cracks with frictional contact, Int. J. Numer. Methods Eng. 121 (4) (2020) 740–762.

[36] Z.Q. Yue, S. Chen, L.G. Tham, Finite element modeling of geomaterials using digital image processing, Comput. Geotech. 30 (5) (2003) 375–397.

[37] Y. Xu, S. Zhao, G. Jin, L. Liang, H. Jiang, X. Wang, Explicit dynamic fracture simulation of two-phase materials using a novel meso-structure modelling approach,

molecular dynamics simulation, Comput. Mater. Sci. 112 (2016) 161–169.

Compos. Struct. 208 (2019) 407–417.

[38] E.J. Garboczi, Three-dimensional mathematical analysis of particle shape using X-ray tomography and spherical harmonics: application to aggregates used in concrete, Cem. Concr. Res. 32 (10) (2002) 1621–1638.

[39] W. Ren, Z. Yang, R. Sharma, C.H. Zhang, P.J. Withers, Two-dimensional X-ray CT image based meso-scale fracture modelling of concrete, Eng. Fract. Mech. 133 (2015) 24–39.

[40] Q. Yu, H. Liu, T. Yang, H. Liu, 3D numerical study on fracture process of concrete with different ITZ properties using X-ray computerized tomography, Int. J. Solids Struct. 147 (2018) 204–222.

[41] P. Arbenz, C. Flaig, On smoothing surfaces in voxel based finite element analysis of trabecular bone, International Conference on Large-scale Scientific Computing, Springer, Berlin, Heidelberg, 2007, pp. 69–77.

[42] Y.B. Zaitsev, F.H. Wittmann, Simulation of crack propagation and failure of concrete, Mater. Constr. 14 (5) (1981) 357–365.

[43] J.P.B. Leite, V. Slowik, H. Mihashi, Computer simulation of fracture processes of concrete using mesolevel models of lattice structures, Cem. Concr. Res. 34 (6) (2004) 1025–1033.

[44] P. Wriggers, S.O. Moftah, Mesoscale models for concrete: homogenisation and damage behaviour, Finite Elem. Anal. Des. 42 (7) (2006) 623–636.

[45] D.A.H. Hanaor, Y. Gan, M. Revay, D.W. Airey, I. Einav, 3D printable geomaterials, Géotechnique 66 (4) (2016) 323–332.

[46] D. Wei, J. Wang, J. Nie, B. Zhou, Generation of realistic sand particles with fractal nature using an improved spherical harmonic analysis, Comput. Geotech. 104 (2018) 1–12.

[47] Z. Qian, E.J. Garboczi, G. Ye, E. Schlangen, Anm: a geometrical model for the composite structure of mortar and concrete using real-shape particles, Mater. Struct. 49 (1–2) (2016) 149–158.

[48] Y. Gan, M. Kamlah, J. Reimann, Computer simulation of packing structure in pebble beds, Fusion Engineering and Design 85 (10−12) (2010) 1782–1787.

[49] X. Tang, C. Zhang, J. Shi, A multiphase mesostructure mechanics approach to the study of the fracture-damage behavior of concrete, Science in China Series E: Technological Sciences 51 (2) (2008) 8–24.

[50] A. Caballero, C.M. López, I. Carol, 3D meso-structural analysis of concrete specimens under uniaxial tension, Comput. Methods Appl. Mech. Eng. 195 (52) (2006) 7182–7195.

[51] B. Sonon, B. Francois, T.J. Massart, A unified level set based methodology for fast generation of complex microstructural multi-phase RVEs, Comput. Methods Appl. Mech. Eng. 223 (2012) 103–122.

[52] P.A. Cundall, O.D. Strack, A discrete numerical model for granular assemblies, Géotechnique 29 (1) (1979) 47–65.

[53] Y. Zhang, Q. Chen, Z. Wang, J. Zhang, Z. Wang, Z. Li, 3D mesoscale fracture analysis of concrete under complex loading, Eng. Fract. Mech. 220 (2019) 106646.

[54] E.J. Garboczi, J.W. Bullard, Contact function, uniform-thickness shell volume, and convexity measure for 3D star-shaped random particles, Powder Technol. 237 (2013) 191–201.

[55] G. Mollon, J. Zhao, 3D generation of realistic granular samples based on random fields theory and Fourier shape descriptors, Comput. Methods Appl. Mech. Eng. 279 (2014) 46–65.

[56] Z. Zhang, X. Song, Y. Liu, D. Wu, C. Song, Three-dimensional mesoscale modelling of concrete composites by using random walking algorithm, Compos. Sci. Technol. 149 (2017) 235–245.

[57] L. Brassart, I. Doghri, L. Delannay, Homogenization of elasto-plastic composites coupled with a nonlinear finite element analysis of the equivalent inclusion problem, Int. J. Solids Struct. 47 (5) (2010) 716–729.

[58] F. Lavergne, K. Sab, J. Sanahuja, M. Bornert, C. Toulemonde, Investigation of the effect of aggregates' morphology on concrete creep properties by numerical simulations, Cem. Concr. Res. 71 (2015) 14–28.

[59] R. Askey, The 1839 paper on permutations: its relation to the Rodrigues formula and further developments. Mathematics and social utopias in France: Olinde Rodrigues and his times. Edited by Simon Altmann and Eduardo. L. Ortiz, Hist. Math. 28 (2005) 105–118.

[60] Q. Du, M. Gunzburger, Grid generation and optimization based on centroidal Voronoi tessellations, Appl. Math. Comput. 133 (2–3) (2002) 591–607.

[61] C.S. Dong, G.Z. Wang, Curvatures estimation on triangular mesh, Journal of Zhejiang University-Science A 6 (1) (2005) 128–136.

[62] J.W. Bullard, Virtual Cement and Concrete Testing Laboratory: Version 9.5 User Guide (No. Special Publication (NIST SP)-1173), (2014).

[63] Y.X. Gan, C. Chen, Y.P. Shen, Three-dimensional modeling of the mechanical property of linearly elastic open cell foams, Int. J. Solids Struct. 42 (26) (2005) 6628–6642.

[64] E.J. Garboczi, V.I. Kushch, Computing elastic moduli on 3-d X-ray computed tomography image stacks, Journal of the Mechanics and Physics of Solids 76 (2015) 84–97.

[65] Z. Yang, W. Ren, R. Sharma, S. McDonald, M. Mostafavi, Y. Vertyagina, T.J. Marrow, In-situ X-ray computed tomography characterisation of 3D fracture evolution and image-based numerical homogenisation of concrete, Cem. Concr. Compos. 75 (2017) 74–83.

[66] E. Roubin, A. Vallade, N. Benkemoun, J.B. Colliat, Multi-scale failure of heterogeneous materials: a double kinematics enhancement for embedded finite element method, Int. J. Solids Struct. 52 (2015) 180–196.

[67] E. Roubin, Meso-scale FE and Morphological Modeling of Heterogeneous Media: Applications to Cementitious Materials, (2013) (Doctoral dissertation).

[68] B.D. Zhao, D.H. Wei, J.F. Wang, Particle shape quantification using rotation-invariant spherical harmonic analysis, Géotechnique Letters 7 (2) (2017) 190–196.

[69] S.V. Borodachov, D.P. Hardin, E.B. Saff, Asymptotics of weighted best-packing on rectifiable sets, Sbornik: Mathematics 199 (11) (2008) 1579.

[70] A.A. Munjiza, The Combined Finite-discrete Element Method, John Wiley & Sons, 2004.

[71] G. Ma, Y. Chen, F. Yao, W. Zhou, Q. Wang, Evolution of particle size and shape towards a steady state: insights from FDEM simulations of crushable granular materials, Comput. Geotech. 112 (2019) 147–158.

[72] D. Wei, B. Zhao, D. Dias-da-Costa, Y. Gan, An FDEM study of particle breakage under rotational point loading, Eng. Fract. Mech. 212 (2019) 221–237.

[73] R.C. Hurley, D.C. Pagan, An in-situ study of stress evolution and fracture growth during compression of concrete, Int. J. Solids Struct. 168 (2019) 26–40.

[74] M.L. Benzeggagh, M.J.C.S. Kenane, Measurement of mixed-mode delamination fracture toughness of unidirectional glass/epoxy composites with mixed-mode bending apparatus, Compos. Sci. Technol. 56 (4) (1996) 439–449.

[75] J.D. Bass, Elasticity of minerals, glasses, and melts, Mineral Physics and Crystallography: A Handbook of Physical Constants 2 (1995) 45–63.

[76] M. Königsberger, B. Pichler, C. Hellmich, Micromechanics of ITZ–aggregate interaction in concrete part I: stress concentration, J. Am. Ceram. Soc. 97 (2) (2014) 535–542.

[77] A. Turon, C.G. Davila, P.P. Camanho, J. Costa, An engineering solution for mesh size effects in the simulation of delamination using cohesive zone models, Eng. Fract. Mech. 74 (10) (2007) 1665–1682.

[78] Q. Fang, D.A. Boas, Tetrahedral mesh generation from volumetric binary and grayscale images, 2009 IEEE International Symposium on Biomedical Imaging: From Nano to Macro, IEEE, 2009, June, pp. 1142–1145.

[79] C. Geuzaine, J.F. Remacle, Gmsh: a 3-D finite element mesh generator with built-in pre-and post-processing facilities, Int. J. Numer. Methods Eng. 79 (11) (2009) 1309–1331.

[80] AS 3600:2018/Amdt 1, Concrete Structures – Section 3 Design Properties of Materials, Standards Australia, 2018.

[81] L. Snozzi, A. Caballero, J.F. Molinari, Influence of the meso-structure in dynamic fracture simulation of concrete under tensile loading, Cem. Concr. Res. 41 (11) (2011) 1130–1142.

[82] S.M. Kim, R.K.A. Al-Rub, Meso-scale computational modeling of the plastic-damage response of cementitious composites, Cem. Concr. Res. 41 (3) (2011) 339–358.

[83] H.L. Wu, J. Yu, D. Zhang, J.X. Zheng, V.C. Li, Effect of morphological parameters of natural sand on mechanical properties of engineered cementitious composites, Cem. Concr. Compos. 100 (2019) 108–119.

[84] Y. Xu, S. Chen, A method for modeling the damage behavior of concrete with a three-phase mesostructure, Constr. Build. Mater. 102 (2016) 26–38.

[85] R.V. Silva, J. De Brito, R.K. Dhir, Tensile strength behaviour of recycled aggregate concrete, Constr. Build. Mater. 83 (2015) 108–118.

[86] N. Otsuki, S.I. Miyazato, W. Yodsudjai, Influence of recycled aggregate on interfacial transition zone, strength, chloride penetration and carbonation of concrete, J. Mater. Civ. Eng. 15 (5) (2003) 443–451.

[87] D. Su, W.M. Yan, Prediction of 3D size and shape descriptors of irregular granular particles from projected 2D images, Acta Geotech. (2019) 1–23.

[88] J. Zheng, R.D. Hryciw, Traditional soil particle sphericity, roundness and surface roughness by computational geometry, Géotechnique 65 (6) (2015) 494–506.

[89] W.B. Fuller, S.E. Thompson, The laws of proportioning concrete, Trans. Am. Soc. Civ. Eng. 59 (1907) 67–143.

[90] J.C. Russ, Fractal Surfaces, Springer Science & Business Media, 2013.

[91] A. Hillerborg, M. Modéer, P.E. Petersson, Analysis of crack formation and crack growth in concrete by means of fracture mechanics and finite elements, Cem. Concr. Res. 6 (6) (1976) 773–781.

[92] X.P. Xu, A. Needleman, Numerical simulations of fast crack growth in brittle solids, Journal of the Mechanics and Physics of Solids 42 (9) (1994) 1397–1434.

[93] H.T.N. Le, L.H. Poh, S. Wang, M.H. Zhang, Critical parameters for the compressive strength of high-strength concrete, Cem. Concr. Compos. 82 (2017) 202–216.

[94] B. Zhao, J. Wang, 3D quantitative shape analysis on form, roundness, and compactness with μCT, Powder Technol. 291 (2016) 262–275.

[95] A.K.H. Kwan, W.W.S. Fung, Packing density measurement and modelling of fine aggregate and mortar, Cem. Concr. Compos. 31 (6) (2009) 349–357.

[96] P. Richard, M. Cheyrezy, Composition of reactive powder concretes, Cem. Concr. Res. 25 (7) (1995) 1501–1511.

[97] B.H. Green, R.D. Moser, D.A. Scott, W.R. Long, Ultra-high performance concrete history and usage by the corps of engineers, Advances in Civil Engineering Materials 4 (2) (2015) 132–143.

[98] B.A. Williams, R.D. Moser, W.F. Heard, C.F. Johnson, D.A. Scott, T.R. Slawson, ... T.D. White, Equipment and Protocols for Quasi-static and Dynamic Tests of Very-High-Strength Concrete (VHSC) and High-Strength High-Ductility Concrete (HSHDC) (No. ERDC-TR-16-13), US Army Engineer Research and Development Center, Vicksburg United States, 2016.